Design and Beam Test Results for the sPHENIX Electromagnetic and Hadronic Calorimeter Prototypes

C.A. Aidala, V. Bailey, S. Beckman, R. Belmont, C. Biggs, J. Blackburn, S. Boose, M. Chiu, M. Connors,
E. Desmond, A. Franz, J.S. Haggerty, X. He, M.M. Higdon, J. Huang, K. Kauder, E. Kistenev, J. LaBounty,
J.G. Lajoie, M. Lenz, W. Lenz, S. Li, V.R. Loggins, E.J. Mannel, T. Majoros, M.P. McCumber, J.L. Nagle,
M. Phipps, C. Pinkenburg, S. Polizzo, C. Pontieri, M.L. Purschke, J. Putschke, M. Sarsour, T. Rinn, R. Ruggiero,
A. Sen, A.M. Sickles, M.J. Skoby, J. Smiga, P. Sobel, P. Stankus, S. Stoll, A. Sukhanov, E. Thorsland, F. Toldo,
R.S. Towell, B. Ujvari, S. Vazquez-Carson, C.L. Woody

Abstract—The super Pioneering High Energy Nuclear Inter-action eXperiment (sPHENIX) at the Relativistic Heavy Ion Collider (RHIC) will perform high precision measurements of jets and heavy flavor observables for a wide selection of nuclear collision systems, elucidating the microscopic nature of strongly interacting matter ranging from nucleons to the strongly coupled quark-gluon plasma. A prototype of the sPHENIX calorime-ter system was tested at the Fermilab Test Beam Facility as experiment T-1044 in the spring of 2016. The electromagnetic calorimeter (EMCal) prototype is composed of scintillating fibers embedded in a mixture of tungsten powder and epoxy. The hadronic calorimeter (HCal) prototype is composed of tilted steel plates alternating with plastic scintillator. Results of the test beam reveal the energy resolution for electrons in the EMCal is $2.8\% \oplus 15.5\%/\sqrt{E}$ and the energy resolution for hadrons in the combined EMCal plus HCal system is $13.5\% \oplus 64.9\%/\sqrt{E}$. These results demonstrate that the performance of the proposed calorimeter system satisfies the sPHENIX specifications.

Index Terms—Calorimeters, electromagnetic calorimetry, hadronic calorimetry, performance evaluation, prototypes, Rel-ativistic Heavy Ion Collider (RHIC), silicon photomultiplier (SiPM), simulation, "Spaghetti" Calorimeter (SPACAL), su-per Pioneering High Energy Nuclear Interaction eXperiment (sPHENIX)

I. INTRODUCTION

The super Pioneering High Energy Nuclear Interaction eXperiment (sPHENIX) is a planned experiment [1] at the Relativistic Heavy Ion Collider (RHIC). RHIC is a highly versatile machine that collides a diverse array of nuclear beams from protons to heavy-ions, and supports a very broad physics program for the study of both hot and cold quantum chromo-dynamics (QCD) matter. sPHENIX is specifically designed for the measurements of jets, quarkonia, and other rare processes originating from hard scatterings to study the microscopic na-ture of strongly interacting matter ranging from nucleons [2] to the strongly coupled quark-gluon plasma (QGP) created in col-lisions of gold ions at $\sqrt{s_{NN}} = 200$ GeV [3]–[6]. sPHENIX is equipped with a tracking system and a three-segment calorimeter system, both of which have a full 2π acceptance in azimuth and a pseudorapidity coverage of $|\eta| < 1.1$. sPHENIX has acquired the former BaBar magnet, which has an inner

radius of 1.4 meters and an outer radius of 1.75 meters [7]. The sPHENIX calorimeter system includes an electromagnetic calorimeter and an inner hadronic calorimeter, which sit inside the solenoid, and an outer hadronic calorimeter located outside of the magnet. The electromagnetic calorimeter will be used for identifying photons, electrons and positrons. Photons can be used to tag the energy of opposing jets traversing the QGP, while electrons and positrons will be used to study quarkonia suppression and to tag heavy flavor jets. The combined EMCal and HCal are used to measure the total electromagnetic and hadronic energy of jets, whose transverse energy range from 10–50 GeV. sPHENIX will be the first detector at RHIC to employ hadronic calorimetry to enable full jet reconstruction at mid-rapidity.

The electromagnetic calorimeter (EMCal) design is based on both mechanical constraints and physics requirements. The principal mechanical constraint for the EMCal is that it must be compact, i.e. both the EMCal and the inner HCal must fit inside the solenoid magnet with enough space remaining for a tracking system. One major physics requirement is that it needs to have a large solid angle with minimal inactive area to enable accurate jet measurements. The second major physics requirement is for the EMCal resolution and segmentation to be compatible with the background conditions in heavy-ion collisions. This means that a small Molière radius and fine segmentation are required to reduce the influence of the underlying heavy ion event background when measuring cluster energy of EM showers.

The most stringent requirement on the EMCal performance is that the energy resolution, when combined with track momentum information, should provide sufficient electron identification to separate the upsilon signal from background. The EMCal resolution requirement for jets is less stringent. In central Au+Au collisions with 0-10% centrality, the average EMCal energy from event background in a typical EMCal tower cluster is 340 MeV [1]. Thus, an EMCal resolution of $15\%/\sqrt{E}$ or better is sufficient to fulfill the sPHENIX physics requirements of measuring photon and upsilon via their di-electron decay channels in relativistic heavy ion collisions at $\sqrt{s_{NN}} = 200$ GeV.

The hadronic calorimeter (HCal) is a sampling calorimeter

with two radial segments: one inside the magnet and the other outside the magnet. The performance requirements of the sPHENIX HCal are driven by the physics specifications related to measuring jets in relativistic heavy ion collisions at $\sqrt{s_{NN}} = 200$ GeV. At the jet energies of interest for the sPHENIX physics program, the energy resolution in central Au+Au collisions is dominated by the underlying event, not the energy resolution of the HCal [1]. The jet energy resolution needed for sPHENIX is $\sigma/E < 120\%/\sqrt{E}$, which corresponds to an energy resolution for single hadrons in the full calorimeter system to be $\sigma/E < 100\%/\sqrt{E}$.

Both the electromagnetic and hadronic calorimeters for sPHENIX are unique in their design in terms of other types of calorimeters that have been built in the past. The EMCal is a so-called SciFi (Scintillating fiber) "Spaghetti" Calorimeter (SPACAL), similar to those which have been used in other experiments [8]–[12]. However, its design uses scintillating fibers embedded in a matrix of tungsten powder and epoxy, and will have a two dimensional tapered geometry that makes it approximately projective back to the interaction vertex in both η and ϕ. Both of these concepts required new and novel techniques in order to carry out its construction. The HCal has its absorber plates parallel to the beam direction, as opposed to being perpendicular to the direction of incident particles, as is typical for most other calorimeters [13]–[15], and allows the outer steel plates to be used as a flux return for the solenoid magnet. The plates are also tilted, with opposite angles in the inner and outer HCals, in order to eliminate the possibility of particles passing through the calorimeter without encountering sufficient absorber (channeling). All of these features make the sPHENIX calorimeter system unique in terms of its overall design, and represent new developments in calorimetry for nuclear and high energy physics.

To verify the design performance, a prototype of the sPHENIX calorimeter system was assembled at Brookhaven National Laboratory and tested at the Fermilab Test Beam Facility (FTBF) as experiment T-1044. A schematic diagram of the T-1044 test beam setup, including the EMCal and HCal prototypes, is shown in Figure 1. The beam goes from left to right in the diagram interacting with the EMCal, the inner HCal, a "mock cryostat" and the outer HCal. The mock cryostat, comprising three vertical plates of aluminum, is placed between the inner and outer HCals to provide as many radiation lengths of material as a particle would encounter traversing the sPHENIX solenoid (approximately 1.4 X_0). This article presents the design of the EMCal and HCal prototypes as well as the results from the T-1044 experiment and simulations.

II. PROTOTYPE ELECTROMAGNETIC CALORIMETER

The EMCal tower design consists of scintillating fibers embedded in the absorber material, which is a matrix of tungsten powder infused with epoxy (W/SciFi). This prototype is based on a design by a group at the University of California Los Angeles (UCLA) [16], [17] and is similar to the SPACAL design used in a number of experiments [8]–[12]. The EMCal towers are designed in "blocks", with two towers composing
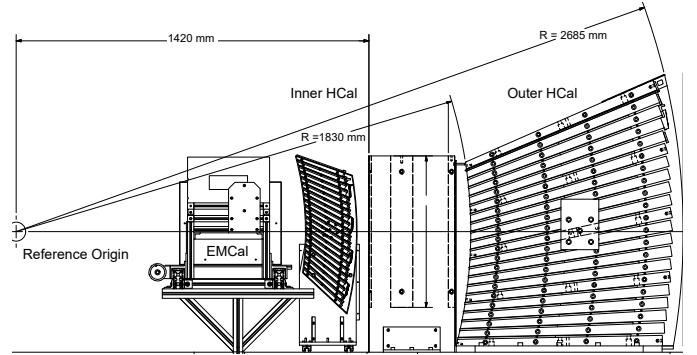

Fig. 1. Schematic diagram of the beam test setup. From left to right, it includes the EMCal, inner HCal, mock cryostat, and outer HCal prototypes.

one block. The blocks are tapered in one-dimension, (ϕ), as shown in Figure 2 for this prototype, which is representative of the sPHENIX calorimeter at central rapidity. For larger rapidities, the blocks will be tapered in two dimensions (η and ϕ). The 2D tapered blocks will be studied in a subsequent beam test which is planned for early 2017.

The back of the two-tower block has a height of 2.39 cm, the front has a height of 2.07 cm, and the total length of the two-tower blocks is 13.9 cm, which corresponds to about 18 radiation length. 1560 scintillating fibers extending along the length direction are embedded in the block. The outer diameter of the fibers is 0.47 mm and the fibers are arranged in a 30×52 triangular lattice with a nominal center-to-center spacing of approximately 1.0 mm. At each of the four sides along the length of the block, the outer most fiber are kept approximately 0.5 mm away from the block surface, forming a skin of absorber to protect the outer fibers from being damaged during the manufacturing process. The density of the whole SPACAL block is approximately 10 g/cm^3, which is about half the density of metallic tungsten. The sampling fraction for EM-showers is about 2.3% and the radiation length $X_0 \approx 0.7$–0.8 cm.
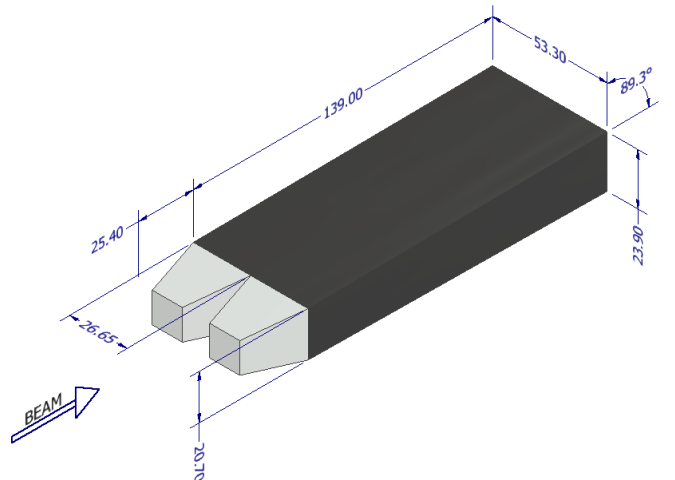

Fig. 2. A SPACAL block (black) with two light guides (gray) attached. Each light guide collects light from a half of the block, and forms a SPACAL tower. All dimension numbers have a unit of mm.

The EMCal prototype consists of 32 two-tower blocks for a total of 64 towers. Each tower is equipped with a light guide on the front face and is read out by four silicon photomultipliers (SiPMs) passively summed into a single preamp/electronics channel. Compared to the full sPHENIX EMCal covering $-1.1 < \eta < 1.1$ and full azimuth, this prototype represents a subset of towers covering $\Delta\eta \times \Delta\phi = 0.2 \times 0.2$ at mid-rapidity.

A. EMCal Block Production

The materials used in the EMCal block production are described in detail in Table I. The tungsten powder used in these blocks comes from Tungsten Heavy Powder Inc., San Diego (THP) and contains small amounts of alloy material. Using a helium pycnometer, THP placed a lower limit on the purity of the tungsten powder at 95.4%. An image of the typical powder particles is shown in Figure 3.
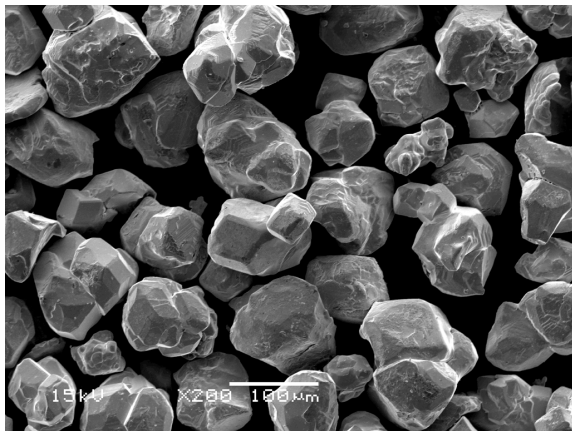

Fig. 3. Tungsten powder was imaged using a JEOL 6060LV General Purpose Scanning Electron Microscope. The powder is sold as Technon Tungsten Powder -100 mesh, with 90% of the particles ranging in size between 25-150 um. This wide distribution allows for higher packing density within each block.

The EMCal blocks were produced at two sites, THP and University of Illinois at Urbana-Champaign (UIUC). To produce the EMCal blocks, the scintillating fibers are placed inside brass mesh screens, which position the fibers in a triangular pattern with a nominal center-to-center spacing of approximately 1.0 mm. The screens are then separated longitudinally, placed in the mold, and tilted to form the taper in one dimension. Tungsten powder is poured uniformly into the mold and then epoxy is poured into the tungsten-fiber matrix. To aid the flow and distribution of epoxy, a light vacuum is applied to the mold at the UIUC production site, while THP used a centrifuge to distribute the epoxy. After 24 hours, the SPACAL block is released from the mold. The blocks are first trimmed with carbide tipped cutters and then with diamond tipped ones. This allows the ends of the blocks to be cut without degrading the light output of the fibers.

B. Light Collection

The EMCal light guide is a machined acrylic trapezoidal prism that fully covers one tower of the W/SciFi two-tower block (2.64×2.36 cm^2) and transitions over a 2.54 cm height

TABLE I
EMCAL BLOCK COMPONENT MATERIALS

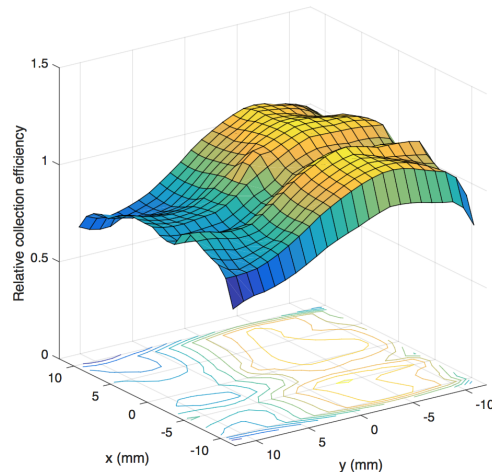| Material	Property	Value
Tungsten powder	THP Technon 100 mesh	
	particle size	25-150 μm
	bulk density (solid)	$\geq$ 18.50 g/cm^3
	tap density (powder)	$\geq$ 11.25 g/cm^3
	purity	$\geq$ 95.4% W
	impurities ($\leq$ 5 percent)	Fe, Ni, O2, Co,
		Cr, Cu, Mo
Scintillating fiber	Kuraray SCSF78	
	(single cladding, blue)	
Epoxy	EPO-TEK 301	

Fig. 4. Relative light collection efficiency for the light guide and SiPM assembly with respect to the input fiber position in X-Y.

to an area (1.4×1.4 cm^2) to accommodate a 2×2 array of SiPMs. The light guides are epoxied to the thin end of the two-tower block. Four SiPMs, mounted on an EMCal preamp printed circuit board, are used to read out the block. The SiPMs are coupled to the light guide using General Electric Silicones RTV615 [18].

To measure the overall efficiency of the light guide, one tower of a W/SciFi block is optically coupled to a 2 inch window photomultiplier tube (PMT). The PMT window fully covers the readout surface of the block, and the readout end of the tower is masked. The analog-to-digital converter (ADC) distribution arising from cosmic rays is measured with trigger counters above and below the block. An acrylic light guide is then optically coupled between the block and the PMT, and the measurement is repeated. Relative to the directly coupled measurement, the light guide measurement yields 71% of the light, which represents the overall efficiency of the light guide.

To map the uniformity of the light guide, a UV-pulse-excited scintillation fiber is scanned through the input end of the light guide and the response is read out using an array of 2×2 SiPMs and preamplifier as in the prototype. The measured relative collection efficiency with respect to the input fiber position in X-Y is shown in Figure 4. The center of the area bounded by the four SiPMs is offset from the center of the

light guide, causing an asymmetry of the collection efficiency with respect to the center of the light guide. Throughout the input cross section of the light guide, $\sim 30\%$ relative variation is observed, which leads to $\sim 20\%$ position dependent energy response variation for electromagnetic showers as discussed in Section VII.

C. Assembly

After the blocks are produced at THP and UIUC, they are assembled at BNL prior to shipping the completed EMCal protoype to Fermilab for the test beam. The blocks are first epoxied together into rows of eight towers in a gluing fixture, which aligns the front readout surface of the blocks in a single plane. Two layers of Vikuiti Specular Reflector Film (ESR) reflective film [19] are then epoxied to the back surface of each of the rows. Light guides are epoxied to the front surface of the row. The preamplifier board, which carries four SiPMs per tower, is used to align the light guides on the towers. The SiPMs are optically coupled to the light guides, and the board carrying the SiPMs is mechanically secured by a screw to the center of each light guide, as shown in Figure 5. Eight rows of EMCal blocks are stacked and placed in a light-tight enclosure box. The preamplifier heat output is 2.5 W/board, necessitating an active cooling system. A blower is used to drive air through the enclosure box, providing sufficient cooling for the preamplifier and SiPM.
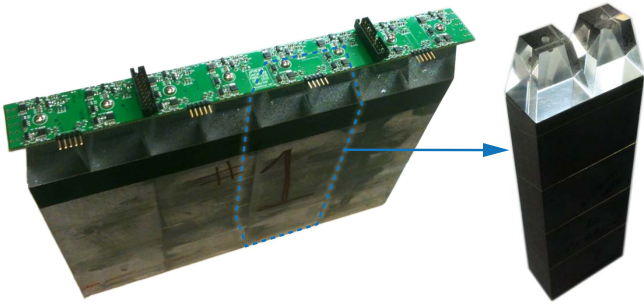

Fig. 5. A row of four EMCal blocks with light guides and preamp board on the left. Among them, one of the blocks and its two light guides are highlighted and displayed separately on the right side.

III. PROTOTYPE HADRONIC CALORIMETER

The inner and outer HCal prototypes are constructed as a small pseudorapidity and azimuthal segment ($\Delta\eta \times \Delta\phi = 0.4 \times 0.4$ at mid-rapidity) of the full scale sPHENIX design, with alternating layers of scintillator tiles and steel absorber plates. The absorber plates are tapered and tilted from the radial direction to provide more uniform sampling in azimuth. Extruded tiles of plastic scintillator with an embedded wavelength shifting (WLS) fiber are interspersed between the absorber plates. The tilt angle is chosen so that a radial track from the center of the interaction region traverses at least four scintillator tiles of each HCal. Each tile is read out at the outer radius with SiPMs. The analog signals from five tiles are summed to a single preamplifier channel to form a single calorimeter tower.

(a) Scintillator tile production for inner HCal
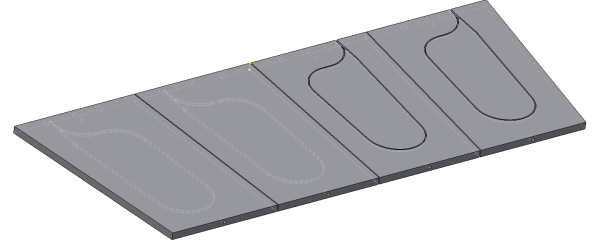
(b) Inner HCal tile design patterns
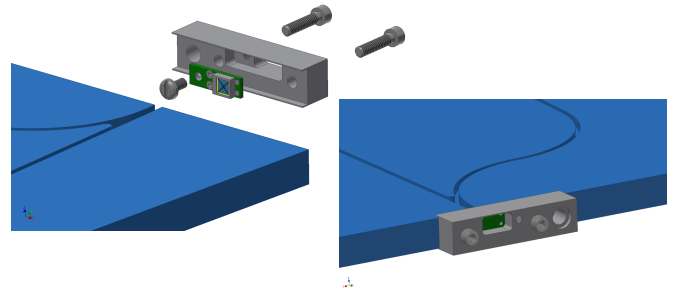
(c) Plastic coupler to attach the SiPM at the fiber exit

Fig. 6. HCal tile production. (a) Inner HCal scintillating tiles in several stages of production. From left to right tiles are machined, then coated and embedded with WLS fiber. (b) 4 scintillating tiles arranged symmetrically around $\eta = 0$ to be inserted between the steel absorber plates. (c) SiPM installation at the fiber exit using a plastic coupler.

TABLE II
PROPERTIES OF THE HCAL SCINTILLATING TILES AND FIBER.

Property	
Plastic	Extruded polystyrene
Scintillation dopant	1.5% of PTP and 0.01% POPOP
Reflective coating	Proprietary coating by surface exposure to aromatic solvents
Reflective layer thickness	50 μm
Wrapping	100 μm Al foil followed by one layer of 30 μm cling-wrap and a 100 μm layer of black vinyl tape
Attenuation length in lateral direction (with respect to extrusion)	Approximately 2-2.5 m
Wavelength shifting fiber Formulation	Single clad Kuraray Y11 200, K-27, S-Type
Cladding material	Polymethylmethacrylate (PMMA)
Fiber diameter	1 mm
Emission peak	476 nm
Fiber core attenuation length	> 2 m
Optical cement	EPO-TEK 3015

The properties of the HCal scintillating tiles are listed in Table II. Figure 6 (a) shows the steps of tile production.

Figure 6 (a,b) and Figure 7 show the inner and outer HCal fiber routing patterns. The Kuraray [20] single-clad fiber is chosen due to its flexibility and longevity, both of which are critical in the geometry with multiple fiber bends. The properties of the HCal wavelength shifting fibers are included in Table II. The fiber routing is designed so that any energy deposited in the scintillator is within a 2.5 cm distance from a WLS fiber, and the bend radius of any turn in the fiber has been limited to 2.5 cm to limit mechanical stress and light loss, based on the experience of the T2K collaboration [21] as well as the experience with the test tiles.
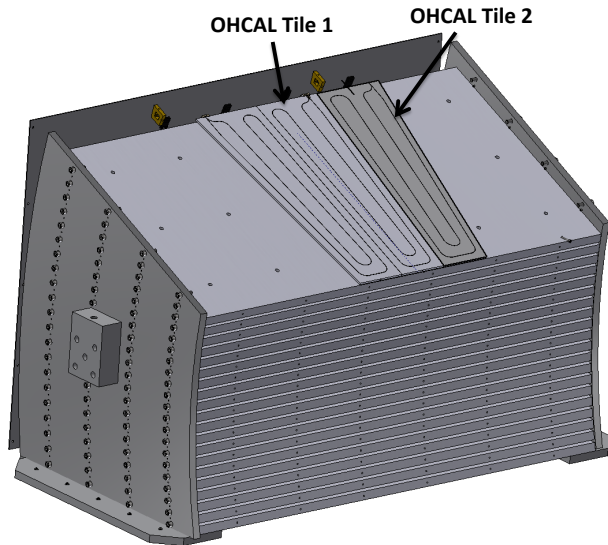

Fig. 7. Schematic diagram of the outer HCal tile designs and assembly. 20 steel absorber plates are stacked together, then 80 scintillating tiles are inserted between them. Tile fiber patterns are shown on the top tiles.

The scintillation light produced in the tiles by ionization from charged particles is kept inside the tile and reflected diffusely by a reflective coating and reflective tile wrapping. The light is absorbed by the fiber embedded in the scintillator. As shown in Figure 6 (c), the two ends of the fiber are brought to the outer edge of the tile where a small plastic mount supports a 3×3 mm^2 SiPM at the fiber exit. The fiber exit is orthogonal to the tile edge and glued at a depth in the tile that allows for installation of the SiPM centered around the fiber exits. The air gap between the fiber ends and the face of the SiPM allows the emitted light to spread over the face of the SiPM, reducing the probability of optical saturation resulting from the two or more photons impinging on the same pixel. A gap of 0.75 mm satisfies the following two requirements: (1) there be no more than a 5% variation in the SiPM response when fibers and SiPM are misaligned by 0.2 mm; (2) no more than 20% loss of the light outside of SiPM sensitive area.

A. Tile Construction

Scintillating tiles for the calorimeter are manufactured by the UNIPLAST Company in Vladimir, Russia. A dry mix of polystyrene granules, p-terphenyl (PTP), and 1,4-bis-2-(5-Phenyloxazolyl)-benzene (POPOP) is melted and extruded,

producing a continuous band of hot scintillating plastic 25 cm wide.

The scintillator is then cut into 2 m long pieces which are inspected for defects and discolorations and, if this low level control is passed, mechanically machined into the tiles according to the specified dimensions. The tiles are then placed in a bath of aromatic solvents resulting in the development of a white diffuse reflective coating over the whole tile surface with an average thickness of 50 μm. This process also removes microscopic non-uniformities normally present on the surface of extruded plastic, which decreases aging and improves the ability of the tile to withstand pressure without crazing. It also enhances the efficiency of light collection in tiles with embedded fibers. Coated tiles are then grooved and WLS fibers are embedded. The fibers are glued using optical epoxy (EPO-TEK 301) with special care given to fiber positioning at the exit from the tile. The fibers are cut at the tile edge and polished by hand.

B. Tile Testing

To determine the light response across the tiles, various studies have been performed. In one setup, an LED with a collimator is attached to a mount on a two-dimensional rail system with very accurate stepper motors. This allows an automated analysis with very high positional precision. The LED scans of the outer HCal tiles consist of 174 points in the long direction (X) and 54 points in the short direction (Y) for a total of 9,396 points. The scan positions are 0.5 cm (approximately the LED spot size) apart in each direction. The principal disadvantage of an LED scan is that light is inserted into the tile directly rather than being induced by ionizing radiation. During the FTBF test beam running, a "tile mapper" was constructed and placed on a two-dimensional motion table. The motion table moves up/down and left/right, keeping the position along the beam direction fixed. The tile mapper included four outer HCal tiles placed perpendicular to the beam direction, so that movement on the motion table corresponds to different positions on the tile face. Each tile is read out individually, which enables a detailed study of the light response as a function of position. The scan consists of 20 total positions, 10 positions focused on the inner part of the tile and 10 focused on the outer part of the tile. A few of the outer scan positions fall near the edge and are excluded from the analysis. This study was performed with the 16 GeV negative pion beam.

Figure 8 shows the LED scan of an outer HCal tile using 405 nm UV LED. Additional scans were performed using 375 and 361 nm UV LEDs with similar results. The overlaid black circles are the beam scan positions on a different tile. The relative positional accuracy of the points is 0.2-0.3 cm. The numbers show the ratio of the average ADC value of the 16 GeV pion data to the average ADC value of the LED scan for that point. The normalization is arbitrarily chosen so that the numerical values are near unity.

Most of the points have ratio values close to unity, indicating good agreement between the 16 GeV pion data and the LED data. The points close to the SiPM, which can be seen as
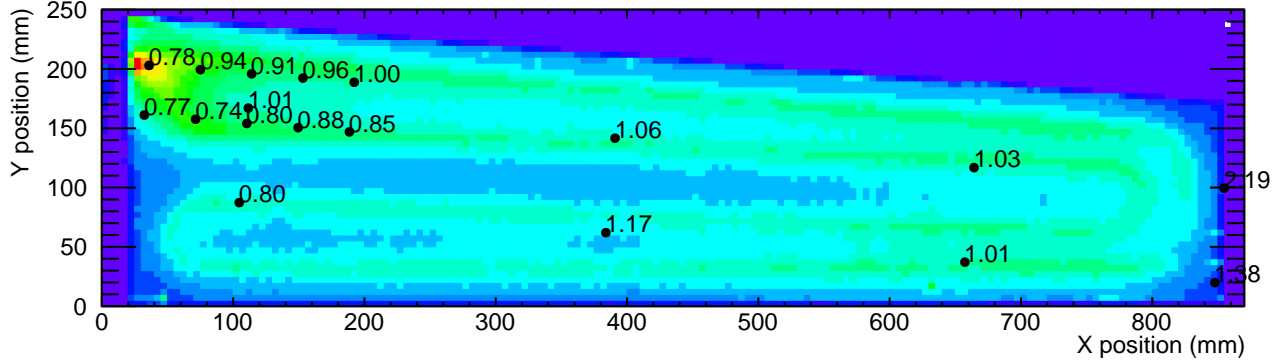
Fig. 8. LED response of a scintillation outer HCal tile with tile mapper scan data overlaid as black points. The numerical value shown at each point is the normalized ratio of the LED response to the tile mapper response.

the red region in the upper left, show a downward trend in the ratio values, suggesting that the intense bright spot in the LED data is not as intense in the 16 GeV pion data. Additionally, the lower set of the five inner points are systematically a little lower than the LED data, and they appear to be right on top of the fiber. This is most likely due to the fact that, in the LED scan, some of the light from the LED is captured directly by the fiber, so there is a modest enhancement directly over the fiber that is naturally not present in the 16 GeV pion data. Both sets of five inner points, however, show a decreasing trend as the points get close to the SiPM.

Figure 9 shows the average ADC value for each scan position as a function of the distance from the SiPM. While the 16 GeV pion data do not show as much of an enhancement near the SiPM as the LED scan, it can be seen that for points less than 15 cm away from the SiPM that there is a strong rise in the average ADC as the distance to the SiPM decreases. This is most likely due to the fact that some of the light in the fiber is carried in the cladding, which has a very short attenuation length, and is therefore lost for most positions in the tile. Studies of small double-ended scintillating tiles have indicated that up to 50% of the light is carried in the cladding, though this is with LED light rather than scintillation light. Here the results indicate that about 33% of the light is carried in the cladding. The area in which more light is collected due to light being present in the cladding is of order 5 cm^2 right around the SiPM mounting, which is at the back of the calorimeter. The spatial density of shower particles is lowest at the back of the calorimeter and therefore this small amount of additional light has a negligible effect on the determination of the shower energy.

C. Geometry

Table III shows the basic mechanical parameters of the inner and outer HCal prototypes. The major components are 20 steel absorber plates and 80 scintillating tiles which are read out with SiPMs along the outer radius of the detector. The SiPMs from five tiles are connected passively to a preamplifier channel. This resulted in a total of 16 towers, 4 in ϕ by 4 in η, equipped with SiPM sensors, preamplifiers, and cables
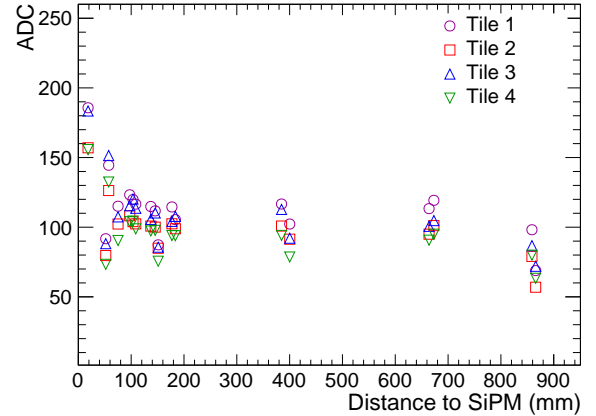

Fig. 9. Outer HCal tile scan using 16 GeV pion beam. Average ADC value in the tile plotted as a function of distance from the SiPM. The points below 150 mm indicate an enhancement close to the SiPM.

TABLE III
DESIGN PARAMETERS FOR THE HADRONIC CALORIMETER PROTOTYPE.

Parameter	Inner/Outer HCal value
Inner radius (envelope)	116/182 cm
Outer radius (envelope)	137/269 cm
Material	ASTM A36 Steel
Number of electronic channels (towers)	16
Absorber plate thickness at inner radius	1.02/2.62 cm
Absorber plate thickness at outer radius	1.47/4.25 cm
Total number of absorber plates	21
Tilt angle (relative to radius)	32/12 °
Scintillator thickness	0.7 cm
Gap thickness	0.85 cm
Sampling fraction at inner radius	0.078/0.037
Sampling fraction at outer radius	0.060/0.028

carrying the differential output of the preamplifiers to the digitizer system. Figure 10 (a) shows the fully assembled inner HCal. Sixteen preamplifier boards corresponding to the 16 towers are visible. In order to make the whole system light tight, the front and back sides were covered with electrically conductive ABS/PVC plastic. This material quickly diverts damaging static charges if there is a buildup. Corners were
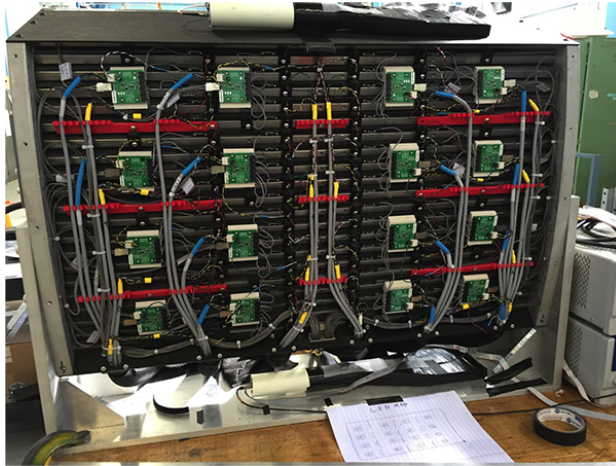
<center>(a)</center>

<center>(b)</center>

Fig. 10. Fully assembled (a) inner and (b) outer HCal. Each section has 20 steel absorber plates stacked together and 80 scintillating tiles are inserted between them. SiPMs read out from five tiles are ganged together as a tower. This results in a total of 16 towers equipped with SiPM sensors, preamplifiers, and cables carrying the differential output of the preamplifiers to the digitizer system.

sealed with light tight black tape. No light leaks were observed during the entire data taking period.

Since the same bias voltage is supplied to all five SiPMs in a given tower, the SiPMs must be gain matched. The SiPMs are sorted and grouped to towers according to the manufacturer's measurements. The SiPM sensors, preamplifiers, and cables are arranged on the outer radius of the inner HCal. The interface boards mounted on the side of the modules monitor the local temperatures and leakage currents, distribute the necessary voltages, and can provide bias corrections for changes in temperature and leakage current.

Figure 10 (b) shows the fully assembled outer HCal. The design of the outer HCal is similar to the inner HCal and the prototype likewise comprises 16 towers. However, since the absorber occupies considerably more radial space, in order to have a minimum thickness of $5.5\lambda_I$ a smaller tilt angle as noted in Table III is needed to preserve the four-tile-crossing geometry. The outer HCal SiPM sensors and electronics were arranged on the outer face of the detector, as seen in Figure 10 (b).

IV. READOUT ELECTRONICS AND DATA ACQUISITION

A. Overview

A common electronics design has been chosen for the readout of the sPHENIX EMCal and HCal detectors using commercially available components. The design uses SiPMs from Hamamatsu as the optical sensors to read out the calorimeters. Signals from the SiPMs associated with a calorimeter tower are passively summed, amplified, shaped, and differentially driven to a digitizer system located near the detector. The signals are continuously digitized at 60 MHz and delayed in a digital pipeline pending a Level-1 trigger from the trigger system. Upon receipt of a Level-1 trigger, the data for 24 time slices corresponding to the triggered event for all towers in the EMCal and HCal are recorded. In addition to the calorimeters, signals from the FTBF beam line Cherenkov counters (used to

tag particular particle species) and finger hodoscopes (an 8 × 8 array of 0.5 cm wide scintillators used to determine the beam position event-by-event) are digitized and recorded. Details of the readout electronics for the calorimeters are discussed in this section.

B. Optical Sensors

The compact nature of the EMCal and HCal detectors and the location of the EMCal and inner HCal inside the 1.4-Tesla solenoidal field of the sPHENIX experiment require that the optical sensors be both physically small and immune to magnetic effects. A device with large gain is also desirable in order to reduce the demands on the performance specifications of the front end analog electronics. SiPMs meet these requirements. For both the EMCal and the HCal, the Hamamatsu S12572-33-015P MultiPixel Photon Counter has been selected as the preferred optical sensor. This device was chosen in order to provide a high pixel count (40K, 15 μm pixels) for good linearity over a large dynamic range along with high-photon detection efficiency ($\sim 25\%$). These SiPMs were operated at voltages approximately 4 volts above the break down voltage in order to maintain a nominal gain of 2.3×10^5.

C. Analog Front End

The preamps used to amplify SiPM signals from both the EMCal and HCal are of the same design, differing only in packaging. The signals from the SiPMs associated with a calorimeter tower are passively summed and then amplified. The amplifier front end is a common-base configuration acting like a transresistance amplifier or "current conveyor." This configuration presents a very low impedance to the SiPMs thereby minimizing any voltage swing on the device. A charge injection circuit is included to generate a fixed test pulse to the amplifier. The signal then passes through gain circuitry which can select either normal gain or a high gain range, 16x

normal for the EMCal and outer HCal and 32x normal for the inner HCal. For the EMCal, the gain range is selectable via slow control, while for the HCal both ranges were recorded during normal data taking. The amplified signal is then shaped with a peaking time of 30 ns for 60 MHz sampling and driven differentially to the external ADC electronics. Figure 11 shows a schematic of the preamp design.
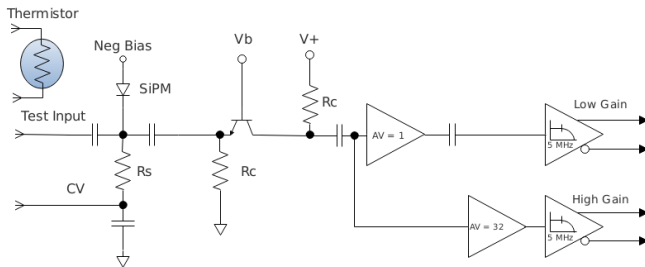

Fig. 11. Schematic diagram for the inner HCal preamplifier. For the EMCal and the outer HCal preamplifier, the high gain channel is ×16 the normal (low gain) channel. In addition, the EMCal design included a programmable selection of either the high gain or normal gain channel as output to the digitizers.

The EMCal preamplifier module consists of eight preamp channels with 4 SiPMs per channel laid out to match the tower geometry of a 1×8 EMCal block. A small surface-mount thermistor is centered between the 4 SiPMs in a tower to monitor the local temperature of SiPMs. Located on the edge of the preamplifier module centered between pairs of EMCal towers are 4 LEDs that are used for monitoring and testing. The SiPMS for the HCal are mounted on small daughter boards that are directly attached to the tiles forming an HCal tower. The five SiPM daughter boards for a tower are connected to an HCal preamp board located on the detector with a short shielded twisted pair cable. An LED is also positioned near each SiPM for monitoring and testing. A thermistor is located near one of the SiPMs in each tower to monitor the local ambient temperature.

D. Slow Control

A slow control system is necessary to provide stable and controllable operational parameters for the SiPMs. The sPHENIX slow control is organized in a tree structure to facilitate the monitoring and control of a large number of channels in the final detector configuration. The slow control system provides: SiPM bias control, SiPM leakage current readback, SiPM temperature measurement, input voltage and voltage regulator temperature, pulse control for both charge injection and LED test pulse, and SiPM temperature and leakage current compensation. The slow control system comprises an interface board and controller board. The interface board, located on the detector, contains ADCs for monitoring temperatures, voltages, and leakage current, and digital-to-analog converters for adjusting the SiPM bias voltage. In addition, the interface board provides power and bias distribution to the preamp boards. For both the EMCal and the HCal, the interface board functionality is the same; however, the packaging is different

to account for differences in geometrical constraints of the two systems. The interface board is connected via a bi-directional serial link to a controller board in a nearby crate. The controller board transmits to the interface board the parameters for gain control, temperature compensation, LED enables, and pulse triggers, and reads back monitoring information. Communication with the controller board is ethernet based.

The controller boards are 6U Ethernet Telnet servers housed in external racks that control the interface boards via isolated RS-485 serial lines over standard CAT5 cables. In addition to providing a monitor and control portal, the controller processes temperature and leakage current values to provide individual SiPM temperature and leakage current compensation if so commanded.

Two controllers are used for the T-1044 Beam Test, one for the EMCal and one for the HCal. A single EMCal interface board serviced the 64 channel EMCal detector. A separate HCal interface board is used for each of the 16 channel Inner and Outer detectors, and the tile mapper. A schematic overview of the slow control system is shown in Figure 12.
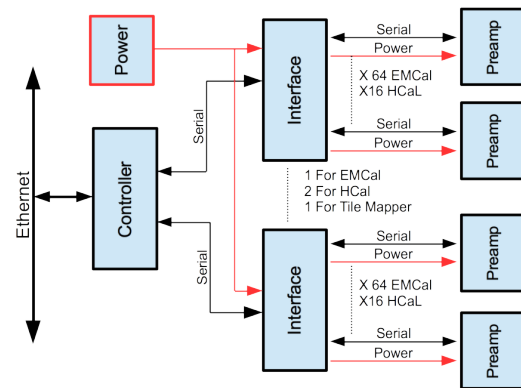

Fig. 12. Schematic overview of the slow control system for the EMCal and HCal. The interface board, connected to the preamp modules, provides environmental monitoring along with power distribution. The controller board receives monitoring data from the interface board and transmits to the interface board slow control commands. Communication with the controller board is ethernet based.

E. SiPM temperature compensation

The gain of an SiPM is sensitive to the temperature. Large variations in gain due to temperature variations can potentially lead to significant uncertainties in determining the energy deposited in the calorimeter. There are several approaches to stabilizing the temperature of the SiPMs or limit the potential temperature variations of the SiPMs. The first approach is to use active cooling to stabilize the temperature to a known temperature using either a Peltier or liquid coolant based system. Another approach is stabilize the temperature using air cooling and to perform corrections to the data to compensate for the variations in gain as a function of temperature. This is the approach that was chosen for the prototype detector. The temperature compensation can be accomplished in one of two ways. Firstly, the slow control system is capable of making online gain adjustments (by adjusting the SiPM bias voltage)
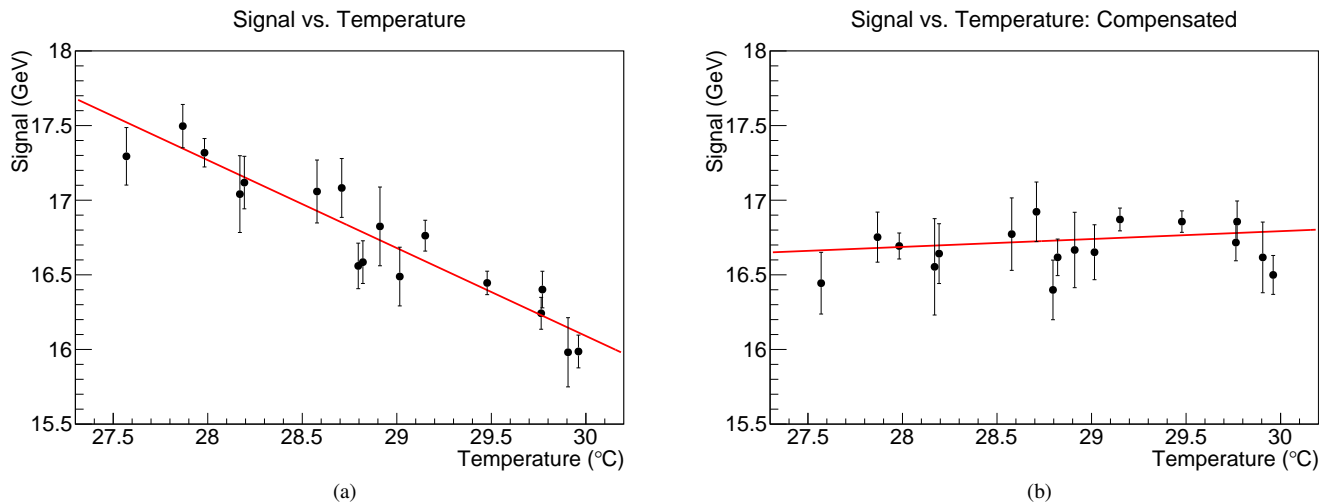
Fig. 13. EMCal SiPM signal vs. temperature without (panel (a)) and with (panel (b)) temperature compensation.

based on the temperatures measured by the thermistors in the front end electronics. Secondly, it is possible to perform an offline correction by determining the temperature dependence of the gain using the recorded data. Temperature data at the SiPMs from the thermistors in the front end electronics are recorded in the data stream. In order to account for data taken at different temperatures, special data was taken to calibrate the temperature correction. Figure 13 shows the calibrated signal (in GeV) vs. the average (event-by-event) temperature across the 5×5 region in the EMCal around a particular tower (note that the temperature may be offset by some constant due to lack of an absolute calibration). Using the calibration data, an offline temperature correction is determined and applied to correct the data. Figure 13 (a) shows example data with no temperature compensation applied, which shows a variation of (-3.68 ± 0.29)%/°C. Figure 13 (b) shows example data with the offline temperature compensation applied. The slope is (0.33 ± 0.30)%/°C, which is effectively consistent with no temperature dependence within the statistical uncertainty.

F. LED Monitoring

To provide monitoring and testing of the calorimeter electronics, an LED pulser system is used. For the EMCal, four 405 nm LEDs are placed on the preamp board such that they are centered between 4 EMCal towers, 2 towers associated with the preamp board and 2 towers associated with the neighboring preamp board. For the HCal, a 405 nm LED is embedded in the edge of each of the five tiles associated with an HCal tower. The LEDs are driven with a fixed amplitude pulse and can be individually pulsed using a programmable driver circuit through the slow control system.

G. Digitizers

The analog signals from the front end amplifiers are transmitted differentially over a 10 m Hard Metrics 16 channel signal cable to a custom digitizing system originally developed for PHENIX [22]. The signals are received differentially and

digitized by a 12 bit flash ADC running at a 60 MHz sampling frequency. The output of the ADC is transmitted to a local FPGA which provides a 4 μs pipeline delay for buffering events for a Level-1 trigger. Upon receipt of a Level-1 trigger, the ADC data for the 24 time samples for the triggered event is transmitted via optical fiber to a PHENIX Data Collection Module (DCM). The formatted data is transmitted to a local computer for logging to disk. The system is designed to operate at the planned sPHENIX maximum Level-1 trigger acceptance rate of 15 kHz.

H. Data Acquisition System

The current data acquisition system in use for most sPHENIX R&D-level efforts is called Really Cool Data Acquisition (RCDAQ) [23]. RCDAQ is client-server based, and can be controlled from multiple clients. There is no "central console" for the operation of the Data Acquisition (DAQ) system. This allows, for example, the DAQ to be started from the beam enclosure while an access is underway to verify the proper state of all components before ending the access. RCDAQ offers an online monitoring stream, which provides the most recent data on a best-effort basis (the online monitoring is not allowed to raise the DAQ busy and throttle the data rate). This monitoring allows any tripped voltage supplies, noisy, or dead channels to be recognized in a timely manner. Additionally, RCDAQ allows the capture of any kind of ancillary data that can be accessed from the DAQ computer, such as temperature readings, voltage levels, and camera pictures. These are embedded in the primary data stream and cannot be separated from the data, and therefore cannot get lost. This additional information provides the ability to perform a "forensics-type" investigation if there is a problematic result or if one finds confusing or incomplete logbook entries.

V. TEST BEAM

Testing of the prototype detectors was performed at the Fermilab Test Beam Facility (FTBF) designated as the T-1044

experiment. The facility has two beamlines which can produce a variety of particle types over a range of energies up to 120 GeV. The T-1044 experiment used the MTest beamline which has two modes of operation; primary protons at 120 GeV and a secondary mixed beam consisting primarily of pions, electrons and muons with energies ranging from 1 to 60 GeV of either positive or negative charge. The beam energies used for T-1044 were secondary beams of 1, 2, 4, 6, 8, 12, 16, 20, 24, and 32 GeV, and primary protons at 120 GeV. The beam is delivered as a slow spill with a 4 sec duration once per minute with a maximum intensity of approximately 10^5 particles per spill. The momentum spread of the beam at the FTBF depends on the beam energy, beam tuning parameters and collimator settings. For our measurements of the calorimeter resolution, these parameters were set to provide a momentum spread of $\approx 2\%\ \Delta p/p$ over the energy range from 2-16 GeV, which is consistent with the value estimated by simulation calculations of the beam line [24], and by our own measurements of the beam with a lead glass detector and by other test beam experiments [16]. The beam spot size is also dependent on the beam energy and tune and ranges from approximately 0.6 cm to several centimeters in size. The secondary beam composition is plotted in Figure 14 showing the relative contribution of electrons, muons and hadrons present in the beam as a function of energy [25], [26]. The kaon content in the beam is expected to be around 1% for beam energies between 20-32 GeV [27].
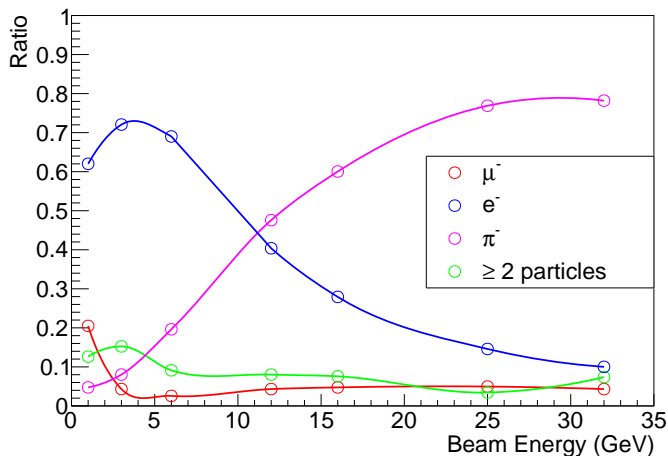

Fig. 14. The relative abundance of particle species present in the FTBF negatively charged beam as a function of beam energy [25].

The FTBF also provides a number of detectors for test beam groups to use. These include two differential gaseous Cherenkov counters upstream of the MTest enclosures, a lead glass calorimeter, multi-wire proportional chambers (MWPC) and trigger counters [25].

The Cherenkov counters are used for offline discrimination between pions and electrons on an event-by-event basis. The gas pressures of the counters are set between the pion and electron thresholds. The inefficiency of the Cherenkov counters resulted in only a few percent contamination for the pion samples.

This experiment used the MT6.2C and MT6.2D areas of the MTest beam line [25]. For the initial tests of the EMCal, the EMCal detector was placed on the MT6.2C motion table. The motion table allowed the detector to be moved with respect to the beam remotely. The EMCal detector is rotated horizontally by an angle of 10 degrees with respect to the beam axis to prevent channeling effects. Additionally, it was also studied at an angle of 45 degrees. For the second half of running, the EMCal was moved to be directly in front of the Inner HCal allowing for combined EMCal/HCal testing. Figure 15 shows a picture of the prototype setup in the MT6.2D area.
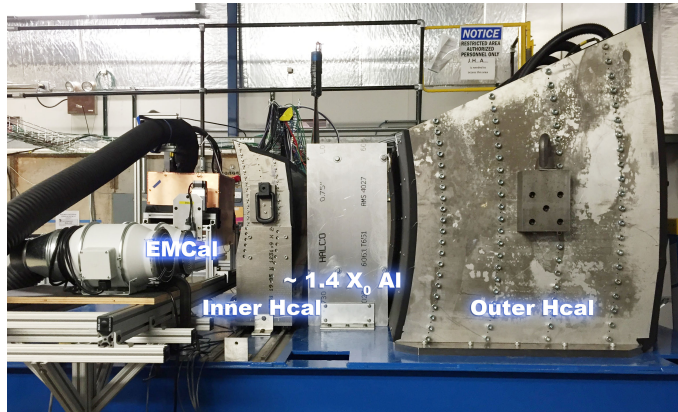

Fig. 15. T-1044 test beam setup is shown where the beam enters the detectors from the left of the image. The EMCal, Inner HCal, mock cryostat of 1.4 X_0 Al and the Outer HCal are all labeled.

A hodoscope and veto counters were installed upstream of the EMCal to allow for the selection of beam particles impinging on the EMCal detector. The hodoscope was provided courtesy of the UCLA group [16], [17] and consisted of 16 0.5 cm finger counters (eight vertical and eight horizontal) read out with SiPMs. The signals from the SiPMs were amplified, shaped, and read out using the digitizers. Four scintillator veto counters surrounded the hodoscope and are read out using PMTs and digitized using the digitizers. If any of the veto counters measures energy above a certain threshold, the event is rejected due to the position of the beam. As shown in Figure 14, a small fraction of events have more than one particle in one event. In order to remove those events, each event is required to have only one valid horizontal and vertical hit in the hodoscope.

A $45 \times 15 \times 15$ cm^3 SF-5 Pb-glass calorimeter is used to double check the test beam energy scale and momentum spread. Pb-glass of this type is known to have a resolution of $(5.6 \pm 0.2)\%/\sqrt{E}$ [28]. The energy resolution was measured at two different operating voltages 1100V and 1200V and obtained the result of $2.0\%(\delta p/p) \oplus 1.4\% \oplus 5.0\%/\sqrt{E}$, as shown in Figure 16.

VI. SIMULATIONS

At this stage of the detector construction the simulation is still under development and subject to validation based on experimental measurements. The sample of results shown in this paper illustrates the methodological approach adopted to achieve a realistic model of the detector performance.
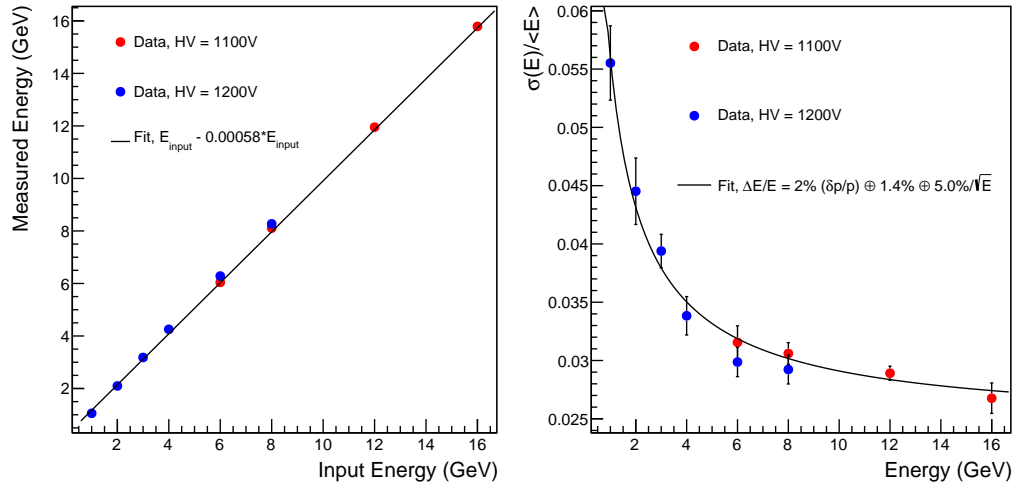
Fig. 16. Pb Glass linearity (left) and energy resolution (right) measured with two high voltage settings of 1100V (red) and 1200V (blue).
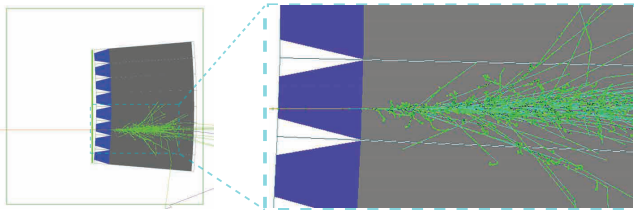

Fig. 17. Side view of an 8 GeV electron shower overlaid with the whole EMCal prototype (left) and zoom-in (right). The incoming electron (red line entering from left) passes through the light guide (blue trapezoid) and develops an EM shower in the W/SciFi EMCal blocks (gray blocks). A 1/10-inch-thick G10 sheet (green vertical plate) is placed before the EMCal to represent the average thickness of the electronics and cooling assembly. Only particles with an energy higher than the critical energy in tungsten (7.8 MeV) are shown.
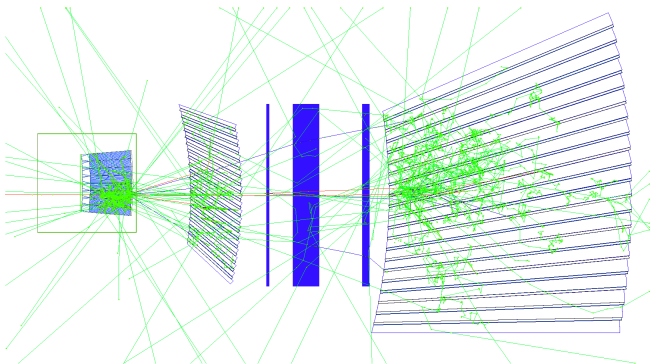

Fig. 18. Side view of a 32 GeV π^- shower as simulated in the EMCal and HCal prototype. The incoming pion (red line on the left edge) starts to develop a shower in the EMCal (left box), which is further absorbed in the inner HCal (tilted plates in the middle), three aluminum plates as a mock up of the sPHENIX magnet (blue block) and the outer HCal (tilted plates on the right side).

The simulation reported here were performed using the pre-defined QGSP_BERT_HP physics configuration distributed in GEANT4 version 4.10.02-patch-01 [29], [30]. Based on the requirements of the sPHENIX experiment and the ongoing validation process, customized physics configurations can be further investigated.

Both the EMCal and the HCal have been simulated using these simulation settings . Their location and internal structure are carefully assigned in order to match that of the actual test beam device. Figure 17 shows typical GEANT4 events of 8 GeV electron showers in the EMCal. Most of the shower particles are contained within the EMCal, and the core of the shower is sampled by multiple rows of fibers. Figure 18 shows a 30 GeV π^- shower in both the EMCal and the HCal prototypes, in which the shower initiates in the EMCal and most shower particles are absorbed by the three segments of calorimeters.

After the GEANT4 simulation stage, digitization was implemented with the following four steps:

1) Energy depositions for each GEANT4 tracklet in the scintillation volume are collected in the sPHENIX analysis framework.

2) The Birks' law of scintillator non-linearity [31] with an ansatz Birks' constant of $k_B = 0.0794$ mm/MeV [32] is implemented to convert ionizing energy deposition to visible energy that is proportional to the expected number of photons produced in the scintillator. The final selection of Birks' constant to be used in sPHENIX simulation still subject to further optimization.

3) The visible energy in each calorimeter tower is summed in a timing window of 0-60 ns to calculate the mean number of active pixels in the SiPM readout. In the case of the EMCal, the sum of visible energy is also modulated by the position of scintillation light production, which accounts for the measured attenuation in the scintillation fiber and the non-uniformity in the light collection efficiency for the light guide as shown in Figure 4. The scale of the mean number of active pixels is set by the mean active pixel count as measured in cosmic tests of the EMCal and HCal. The actual active pixel number is a random number following a Poisson

distribution with a parameter of the mean number of active pixels.

4) In the last step, the ADC for each readout channel is proportional to the sum of the actual active pixel number and a random number following the pedestal distribution. The sum is scaled to an ADC value using measured pixel/ADC value from cosmic tests and discretized to integer ADC value.

The sPHENIX simulations have been integrated with the sPHENIX software framework [33], enabling the same analysis software setup to be used to analyze both the simulated and the beam test data. The simulated data are compared with the real data as discussed in Section VII.

VII. RESULTS

The data from the test beam T-1044 at Fermilab are studied for three different configurations. First, the EMCal is tested as a standalone calorimeter, then the inner and outer HCal are tested, and finally all three calorimeters are tested together as a calorimeter system. For each of these combinations, energy linearity and resolution are measured at selected beam energies. The resolution data points, $\sigma(E)/\langle E \rangle$, are then fit with empirical parametrization functions of the beam energy, E, which are quadratic sums of constant and statistical terms, $\sigma(E)/\langle E \rangle = \sqrt{a^2 + b^2/E}$. For each fit, the p-value for the hypothesis of the fit function is calculated using the χ^2 goodness-of-fit test, assuming the goodness-of-fit statistics follows a χ^2 p.d.f. with the degree of freedom as the number of data points minus two (the number of free fit parameters) [34]. We consider a fit with p-value > 0.05 would indicate the data follow the empirical parametrization within its statistical uncertainty. Meanwhile, we do not expect these curves to describe linearity and resolution with high precision, while the key point for the comparisons and parameterizations is to demonstrate we can describe the general trends of these data. Therefore, for the case where p-value< 0.05, we would conclude the data suggest additional features of energy dependence than these simple parametrizations. However, the parametrization is still valid for qualitatively comparing to the performance specifications of sPHENIX and to other calorimeter systems parameterized in the same way.

A. EMCal Calibration and Check

The relative variation of energy response for EMCal towers is calibrated using minimum ionizing particle (MIP) calibration runs. In these data, the EMCal is rotated downward from its nominal position with the beam passing perpendicular to the EMCal towers. The beam is centered on one column per run, such that the beam passes through all 8 towers in a column. In order to avoid events in which a proton has initiated hadronic showers in the EMCal, the MIP calibration events are selected by requiring signals above the pedestal for each tower in the column of interest and no counts above the pedestal for all other towers. The ADC spectrum for each tower in the column of interest is fit with a Gaussian+Laundau function. The MIP peak ADC value is extracted from each fit as the ADC value corresponding to the maximum point of the fit curve. After

repeating this study for all eight columns, the MIP peak ADC for all towers are collected as shown in Figure 19. Four towers in the middle of row-7 show higher response in the MIP amplitude. This observation was confirmed by sending the beam from row-0 to row-7 and in the reverse direction for each column of towers. The calibrated energy as shown in Section VII-B is corrected for the relative variation of energy response for EMCal towers by dividing the raw ADC of each tower with its MIP peak ADC prior the sum of the tower-cluster energy.
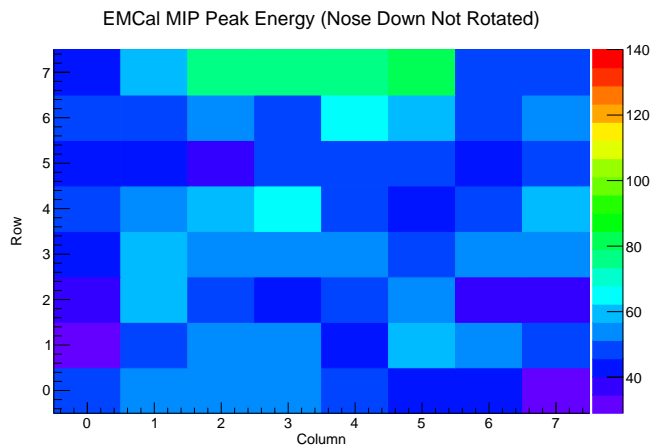

Fig. 19. EMCal MIP peak ADC for each EMCal tower index in columns and rows, used for energy calibration. See text for details.
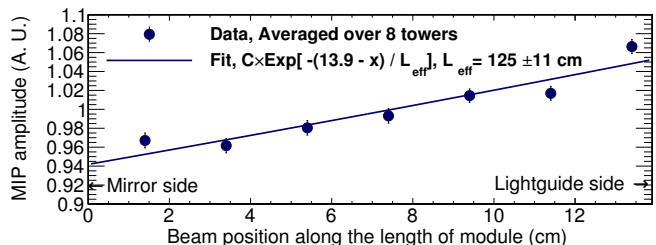

Fig. 20. EMCal MIP peak amplitude plotted against the beam position along the length of module. The data points, which are the average response from eight towers, are fit with an exponential function (curve).

In order to quantify the attenuation of scintillation light inside the EMCal blocks, a 120 GeV proton beam is scanned along the longitudinal direction of the towers in the same setup as the above MIP calibration. The beam traverses the EMCal perpendicular to the length of the block from the non-tapered side of the EMCal block. The MIP signal amplitude is plotted versus the beam position along the block length dimension as in Figure 20. The data points are fit with an exponential function to extract the effective attenuation length of scintillation light in the block, L_{eff}. The result is $L_{\text{eff}} = 125 \pm 11$ cm, which is much longer than the length of the block. This longitudinal position dependent scintillation light yield is used in the simulation in order to describe scintillation light propagation inside the EMCal.
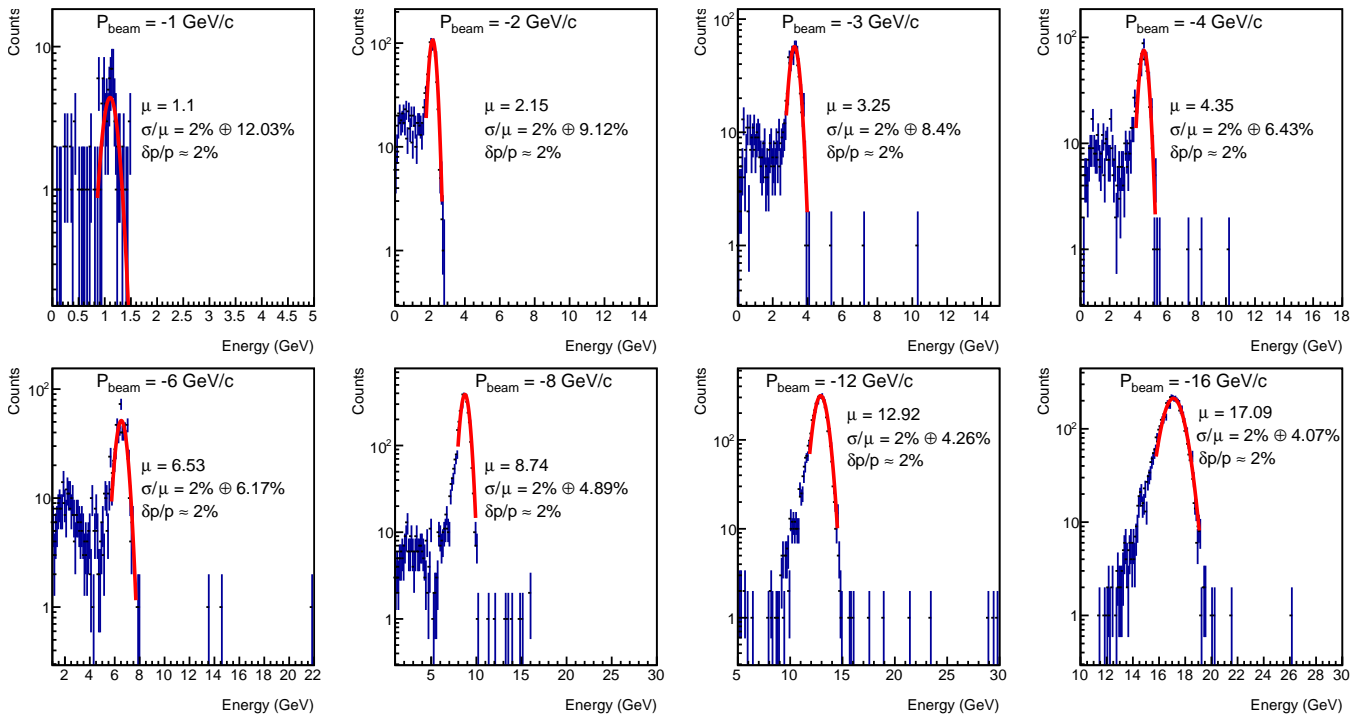
Fig. 21. Cluster energy distribution of electron showers in the EMCal (blue points), for which the beam incident angle is 10 degrees and a 0.5×0.5 cm^2 beam cross section is selected at the center of one EMCal tower. The central tower and most near-by tower are produced at UIUC. For each panel, data for one choice of beam energy is selected as shown in the title, and the energy resolution prior to unfolding a beam momentum spread ($\delta p/p \approx 2\%$) is extracted with a Gaussian fit at the electron peak (red curve). Low energy tails stemming from multi-particle background are excluded from the fit.

An upper limit on the Cherenkov background, produced when charged particles pass through the acrylic light guides, is estimated using dedicated runs in the test beam. With the EMCal towers rotated perpendicular to the incoming beam, 120 GeV protons are set to pass through a column of light guides or a column of SPACAL towers. Events in which a proton initiates a hadronic shower are rejected by vetoing events with non-zero energy in the EMCal towers other than the column being studied. The mean energy from the Cherenkov background when the proton beam passes through the light guide is found to be less than 11% (90% C.L.) of the MIP energy when a proton passes perpendicularly through the EMCal towers. Since in the nominal orientation of the EMCal, the incoming particle travels away from the photon sensor, the Cherenkov background during physics data taking is expected be significantly smaller than this estimated upper limit.

B. EMCal Measurements

The electromagnetic energy resolution for the EMCal is obtained using the electron component of the test beam, which is selected using the Cherenkov detectors, tuned to produce a signal for electron events, but not for hadrons and muons. However, due to multiple particle events as discussed in Section V, the lower energy electron events still contain a fraction of hadrons and muons, which are further rejected using the EMCal energy response. For each event, the calibrated EMCal tower energy is summed within a 5×5 tower cluster centered around the tower with the maximum energy. When selecting a 0.5×0.5 cm^2 beam cross section around the center of

one tower, the 5×5 tower cluster energy is histogramed in Figure 21. The center of the tower is determined by selecting the hodoscope position with the highest average energy response in the EMCal. The mean energy and spread of the EMCal response at each beam energy is extracted with a Gaussian function fit at the electron peak . A beam momentum spread ($\delta p/p \approx 2\%$) is quadratically subtracted from σ/μ of the fit, in order to unfolded beam momentum spread from the relative energy resolution. The Gauss function parameter of μ and energy resolution from each fit are plotted against the nominal beam energy as linearity and resolution. Two types of electron responses are studied:

- The energy resolution for showers located at the center of one tower, which is a test of the intrinsic performance of the W/SciFi sampling structure with minimal sensitivity to the light collection uniformity and tower edge effects. With a 1.0×0.5 cm^2 beam hodoscope selection around the center of one tower, the linearity and resolution are shown in Figure 22 for SPACAL towers produced at UIUC and THP, respectively. At a 10 degree incident angle, the performance of the UIUC and THP SPACAL towers appear qualitatively comparable with each other and with that of simulation, producing a resolution of $\Delta E/E = 1.6\% \oplus 12.7\%/\sqrt{E}$ after unfolding the beam momentum spread. At a 45 degree beam incident angle, the resolution is found to be $\Delta E/E = 12.1\%/\sqrt{E}$ (with a small constant term when compared with the fit uncertainty) after unfolding the beam momentum spread.
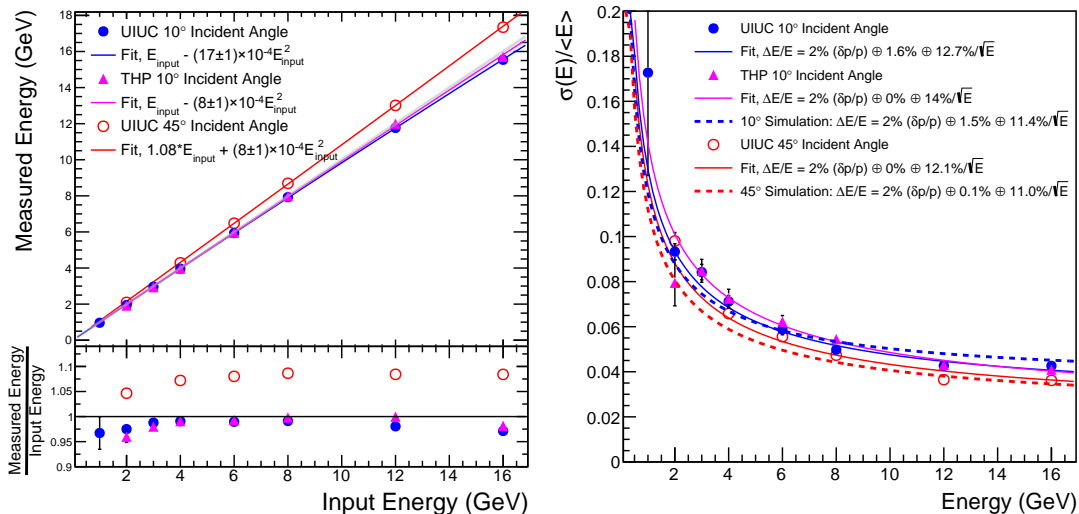- Resolution with a beam cross section selection of

Fig. 22. Linearity and resolution of electron showers in EMCal towers produced at UIUC and THP, for which a 1.0×0.5 cm^2 beam cross section is selected at the center of one EMCal tower. The beam incident angles are 10 degrees (blue) and 45 degrees (red). Data (points) are fit with linear (left solid curves) and $\Delta E/E = \sqrt{a^2 + b^2/E}$ function with results labeled on plot (right solid curves), which are compared with simulation (dashed curves). A beam momentum spread ($\delta p/p \approx 2\%$) is unfolded and included in the resolution.
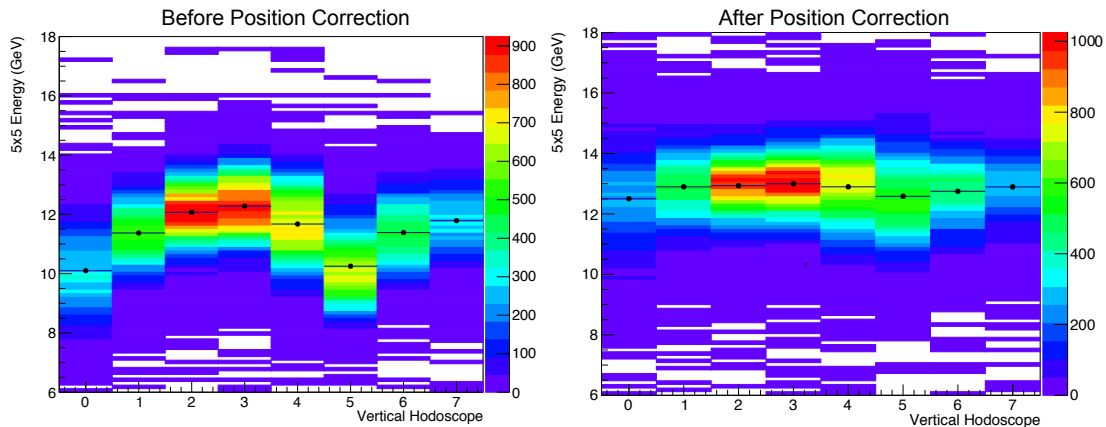
Fig. 23. Cluster energy vs. vertical hodoscope in the EMCal towers produced at UIUC before and after the position-dependent energy correction is applied. The beam energy shown is 12 GeV with an incident angle of 10 degrees. Data is shown prior to unfolding a beam momentum spread ($\delta p/p \approx 2\%$).

2.5×2.5 cm^2, which matches the full cross section of one SPACAL tower and is more relevant for the EMCal performance in sPHENIX. The energy response of the EMCal depends on the hit position of the incoming particle, which mainly stems from the non-uniformity of light collection on the tower light guide and the absorber skin of SPACAL blocks as discussed in Section II. The absorber skin of SPACAL blocks also leads to lower average sampling fraction when compared with that for the center of the block, and therefore, worse statistical term in the energy resolution. A position dependent energy scale correction is applied to the current data based on the two-dimensional beam position as measured using a 0.5×0.5 cm^2 hodoscope selection. Figure 23 shows the performance of position-dependent

energy correction, which clearly reduces the variation of the EMCal energy response. Figure 24 shows the result linearity and resolution for a sum of all electron events within a 2.5×2.5 cm^2 beam cross section after this correction is applied to the EMCal blocks produced at UIUC and THP, respectively. The EMCal resolution after unfolding the beam momentum spread is $\Delta E/E = 2.8\% \oplus 15.5\%/\sqrt{E}$ at a 10 degree beam incident angle and $\Delta E/E = 14.6\%/\sqrt{E}$ (with a small constant term when compared with the fit uncertainty) at a 45 degree beam incident angle.

For both Figure 22 and 24, the linearity response at an incident angle of 45 degrees is approximately 10% higher than at 10 degrees. This difference is expected, since at larger angles, the total energy of the shower is contained more in the narrow
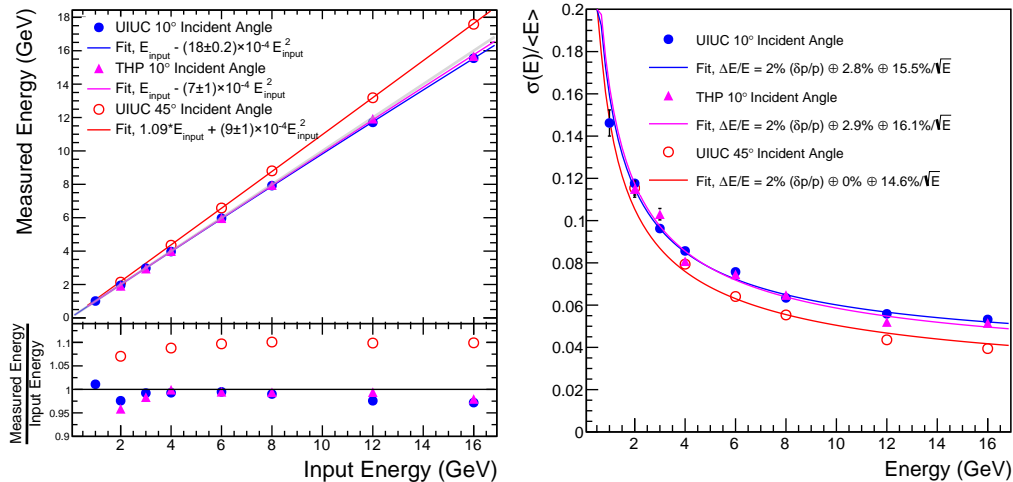
Fig. 24. Linearity and resolution of electron showers in EMCal towers produced at UIUC and THP, for which a 2.5×2.5 cm^2 beam cross section is selected and matches the area of one EMCal tower. The beam incident angles are 10 degrees (blue) and 45 degrees (red). Data (points) are fit with linear (left solid curves) and $\Delta E/E = \sqrt{a^2 + b^2/E}$ function with results labeled on plot (right solid curves). A beam momentum spread ($\delta p/p \approx 2\%$) is unfolded and included in the resolution.

end of the SPACAL towers where the fiber density, and hence the sampling fraction is higher. For 2–3 GeV beam energies, the linearity deviates slightly from the perfect linearity due to the uncertainty in the actual beam energy from the nominal beam energy setting. This variation was also observed with the Pb-glass calorimeter. At higher energies, the measured energy deviates systematically below the nominal beam energy due to back leakage from the calorimeter modules. With the second order polynomial fit, the maximum deviation of the linearity parameterizations from data is within 5% for beam energy larger than 4 GeV.

An important function of the EMCal in sPHENIX is to provide electron identification and hadron rejection for charged tracks. The hadron rejection factor is quantified as the ratio between the total number of incident hadron and the subset of those with an EMCal cluster passing a minimal E/p cut, as measured and simulated in Figure 25. The accepted beam impact points cover an area of 2.5×2.5 cm^2 as tagged by the hodoscope detector. The hadronic beam particles are selected by requiring no activity in the beam-line Cherenkov detectors, which are tuned to produce Cherenkov signals on electrons but not on hadrons and muons. Based on Figure 14, the expected muon component in the beam is simulated and statistically subtracted from the cluster energy spectrum. We note that the muon simulation on EMCal is not directly validated with this test beam. Therefore, this subtraction could lead to a component in the systematic uncertainty for the hadron rejection results, which is still to be investigated. The resulting EMCal cluster energy spectrum for hadrons is integrated from various cut values to the maximum energy in order to estimate the number of hadron events with cluster energy larger than the cut. Its ratio to the total number of hadron events is plotted as inverse of the hadron rejection factor versus minimal cluster energy cut as shown in Figure 25. This hadron sample contains mainly π^-. The kaon content is expected to be very
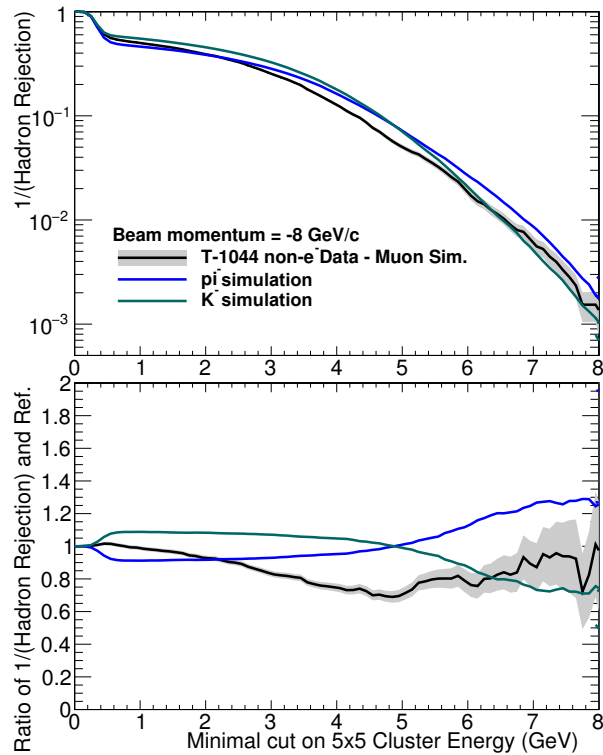

Fig. 25. Hadron rejection plotted against minimal cuts on 5×5 tower cluster energy for negatively-charged beam with momentum of 8 GeV/c. The T-1044 hadron data (black curve with statistical uncertainties in gray), which are non-electron data with the expected muon contribution subtracted, are compared with π^- and K^- simulated curves . The beam momentum spread of around 2% is present in both data and simulation.

small, about 1% of beam content at higher momenta (20–30 GeV/c) [27], and lower at lower momenta (4–12 GeV/c) due to the decay of kaons in flight. Nevertheless, for the

completeness of the study, both π^- and K^- are simulated . The result with beam momentum of 8 GeV/c is shown in Figure 25 as a typical result, while this study is performed in a negatively charged hadron beam momenta of 4, 8 and 12 GeV/c.

C. HCal Calibration

The initial HCal calibration was performed using cosmic MIP events in order to equalize the response of each tower. A set of cosmic MIP events was recorded prior to the test beam data taking in order to calibrate the detector. The cosmic MIP events were triggered with scintillator paddles positioned at the top and bottom of the HCal (in the ϕ direction as seen from the interaction point). In each run, four vertical towers are scanned from top to bottom (e.g. Tower 0–3 in Figure 26). This yields eight individual runs in order to fully calibrate both the inner and outer HCal sections. Figure 26 (a) shows the ADC distributions in the 4×4 inner HCal towers. Each spectrum is fit with the sum of an exponential and a Landau distribution, where the exponential function corresponds to the background and the Landau function represents the MIP events. As seen in the figure, the background component is relatively small. Clear cosmic MIP peaks are observed in all towers.

The corresponding simulation of cosmic muons is performed with 4 GeV muons (corresponding to the mean muon energy at sea level) moving from the top to bottom of the HCal prototype with the GEANT4 setup discussed in Section VI. Figure 26 (b) shows energy deposition in only one column of towers. The mean energy deposited by the cosmic muons in each tower is approximately 8 MeV for the inner HCal. Because of the tilted plate design, towers at the bottom of the inner HCal have more deposited energy than the top ones. This feature was first observed in data and then confirmed by the simulations. This simulation was used to calibrate the ADC signal height in each tower, $I(ch)$, towards the corresponding energy deposition in the test beam:

$$E(ch) = I(ch) \frac{E_{dep}^{cosmic}(ch)}{E_{dep}^{ADC}(ch) \times SF(muon)}, \tag{1}$$

where $E_{dep}^{cosmic}(ch)$ is the total deposited energy extracted from the GEANT4 cosmic simulations, $E_{dep}^{ADC}(ch)$ is the ADC signal height measured from cosmic data, and $SF(muon)$ is the muon sampling fraction. Note that the final energy scale is not set by the cosmic calibration alone but rather by a balancing procedure described in the following sections. Additional studies to further validate the cosmic simulations are still underway.

D. HCal Standalone Measurements

The HCal standalone data are collected with only inner and outer sections of HCal in the beam line and no EMCal in front. In this configuration, electromagnetic showers generally start earlier in the calorimeter and deposit most of their energy in the inner HCal. The hadronic showers, however, are typically deeper than the electromagnetic showers and deposit most of their energy in the outer HCal. The beam is adjusted to be in the middle of the prototypes in order to maximize the hadron shower containment in the 4×4 inner and outer HCal towers. Data were collected with a negatively charged particle beam with energies between 2 GeV and 32 GeV, which contain mainly electrons and pions as shown in Figure 14. Electron and pion events were tagged using the two beamline Cherenkov counters. Hodoscope and veto cuts were applied depending on the beam location, similar to the EMCal analysis, but found no large dependence of the energy resolution on the beam position. Both high and low gain signals from the HCal towers were collected but only low gain channels are used for analysis.

The energy from all of the towers of both the inner and outer HCal are summed to determine the reconstructed energy:

$$E_{HCAL} = Gain_{inner} E_{inner} + Gain_{outer} E_{outer} \tag{2}$$

where E_{inner}, E_{outer} are sum of the calibrated tower energy, $\Sigma_{ch} E(ch)$, within the inner and outer HCal, respectively. The asymmetry between the two sections is defined as

$$A_{HCAL} = \frac{E_{inner} - E_{outer}}{E_{inner} + E_{outer}}. \tag{3}$$

The gain calibration constants, $Gain_{inner}$ and $Gain_{outer}$, are determined in order to minimize the dependence of E_{HCAL} on A_{HCAL} and the deviation of E_{HCAL} from the beam energy. The same gain calibration constants are used in analysis of all beam energies.

Figure 27 shows the reconstructed hadron energy in data and simulation. The beam momentum spread is not unfolded in both cases. At lower energies, hadron measurements are poor due to lower fractions of hadrons in the beam (Figure 14) as well as the increased beam size. The peak at the lower energies in the data corresponds to the small fraction of muons events that pass through the HCal leaving only the minimum ionizing energy. The corresponding hadron resolution and linearity are shown in Figure 28. The data are fit with the function, $\Delta E/E = \sqrt{a^2 + b^2/E}$, as labeled on the plot. A beam momentum spread ($\delta p/p \approx 2\%$) is unfolded and included in the resolution calculation. The hadron energy resolution follows an empirical formula $11.8\% \oplus 81.1\%/\sqrt{E}$ with a p-value of 0.37. The HCal was calibrated for hadronic showers and then used to measure electron showers. The electron resolution for the standalone HCal is $8.1\% \oplus 31.3\%/\sqrt{E}$. This demonstrates the HCal's ability to assist the EMCal by measuring the electron energy leaking from the EMCal into HCal.

As seen in Figure 28 (a), the hadron energy response can be qualitatively described by a linear fit where the reconstructed energy is the same as the input energy. The bottom panel shows the ratio between the reconstructed energy and the fit. The 4 GeV hadron measurement is poor because the hadron peak is difficult to distinguish from the muon MIP peak as seen in Figure 27 due to their proximity. The electrons can be described with a second order polynomial where the second order coefficient is $0.012 \pm 8.8 \times 10^{-5}$. The ratio between the electron data and the fit are also shown in the bottom panel of Figure 27. Furthermore, Figure 29 shows the HCal
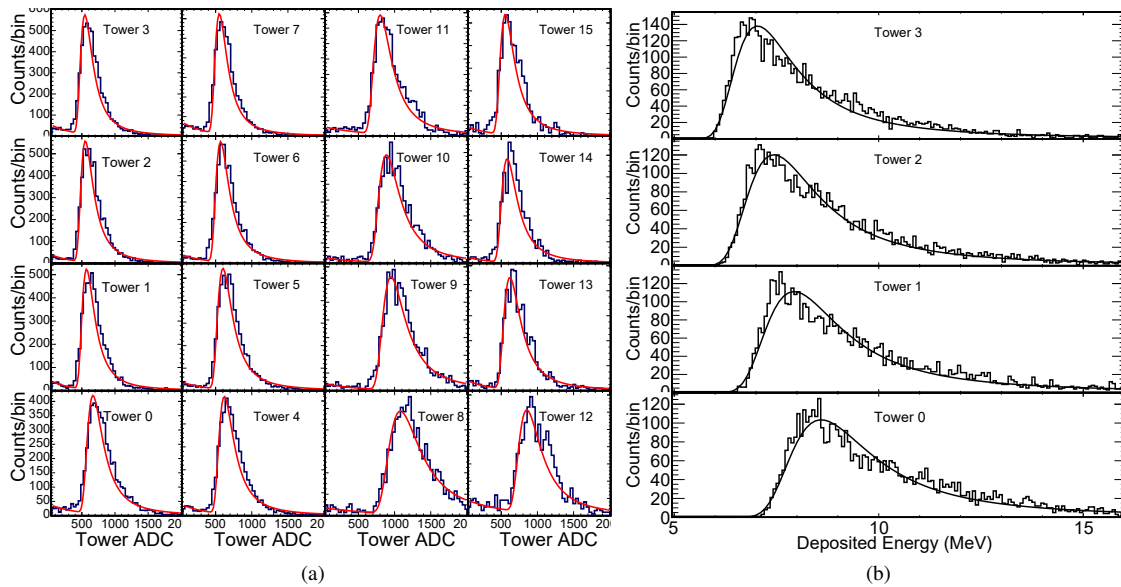
Fig. 26. Tower to tower calibration for inner and outer HCal was done with cosmic muons. (a) Measured raw ADC spectra of cosmic ray muon events in the inner HCal. (b) Inner HCal cosmic muon energy deposition in simulation in one column. Muons were simulated at 4 GeV moving from the top to bottom. Energy depositions in the bottom towers are higher due to the tilted plate design where muons have to go through a longer path through the scintillating tiles.
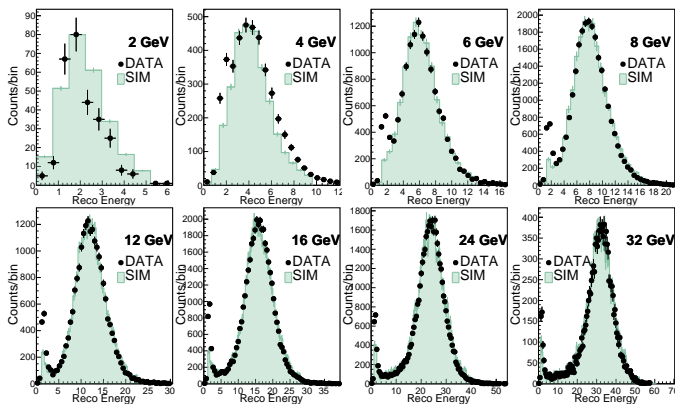

Fig. 27. Hadron reconstruction in standalone HCal setup. Calibrated 4×4 tower energies were added together from the inner and the outer HCal. The simulation is shown by the filled histogram and the solid points are the data. The peak at the lower energies in the data corresponds to the small fraction of muon events that pass through the HCal leaving only the minimum ionizing energy, which were not simulated.

$\langle E_e \rangle / \langle E_\pi \rangle$ response as function of the beam energy, which is always higher than 1 and is energy dependent.

E. Hadron Measurement with sPHENIX Configuration

The full hadron measurement is done with the sPHENIX configuration, which includes all three segments of calorimeters including the EMCal in front of the HCal. In this configuration the total energy will be reconstructed by summing up the digitized data from both the EMCal and the HCal. The development of hadronic showers is a complicated process with significant fluctuations of the reconstructed energy compared to electromagnetic showers. Distinguishing the shower starting position helps to understand the longitudinal shower development fluctuations. Therefore, in this analysis, the events are sorted into three inclusive categories depending on their longitudinal shower profile:

- *HCALOUT*: Events where hadrons pass through the EM-Cal and inner HCal and primarily shower in the outer HCal alone or pass through the full calorimeter system without showering. These events are shown as the blue points in Figure 30.
- *HCAL*: Events where hadrons pass through the EMCal. In these events, hadron showers start in the inner HCal, or the outer HCal, or pass through all three calorimeters. These events are shown as red points in Figure 30.
- *FULL*: This represents all hadrons irrespective of when they start showering. They are shown as black points in Figure 30. These include hadron showers that start in the EMCal, inner HCal, outer HCal, or pass through all three calorimeter systems.

These event categories help diagnose each section of the calorimeters independently as well as understanding of the leakage variations, shower containment and longitudinal fluctuations depending on their starting position. The EMCal energy was balanced with respect to the HCal in a similar way by changing the gain factors prior to summing them into the total reconstructed energy, E_{Total} according to:

$$E_{Total} = Gain_{EMCal} E_{EMCal} + Gain_{HCal} E_{HCal} \quad (4)$$

where E_{EMCal} is the sum of the calibrated tower energy within the EMCal. The procedure of adjusting the gain coefficients is very similar to the one described in the last section for balancing inner vs outer HCal: $Gain_{EMCal}$ and $Gain_{HCal}$ are adjusted in order to minimize the dependence of E_{Total} on $(E_{EMCal} - E_{HCal})/(E_{EMCal} + E_{HCal})$ and the deviation of E_{Total} from the beam energy. The FULL shower sample is used for this calibration. The HCal gains were held fixed
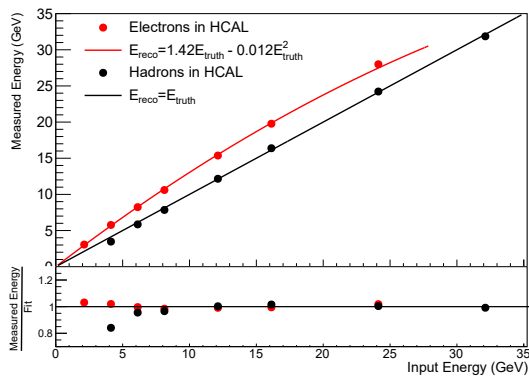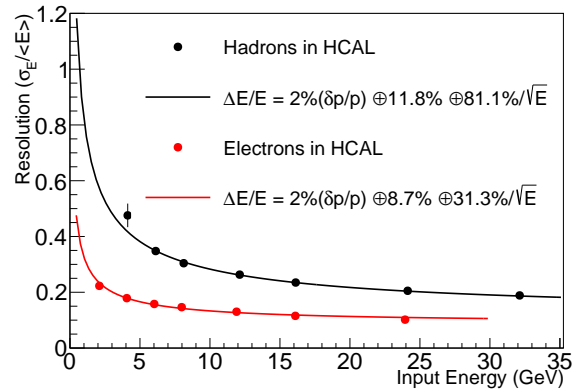
Fig. 28. HCal standalone measurements without the EMCal in-front. (a) HCal linearity for electrons and hadrons. The lower panel shows the ratio of reconstructed energy and the fits. (b) Corresponding HCal resolution for hadrons and electrons. The beam momentum spread ($\delta p/p \approx 2\%$) is unfolded and included in the resolution calculation.
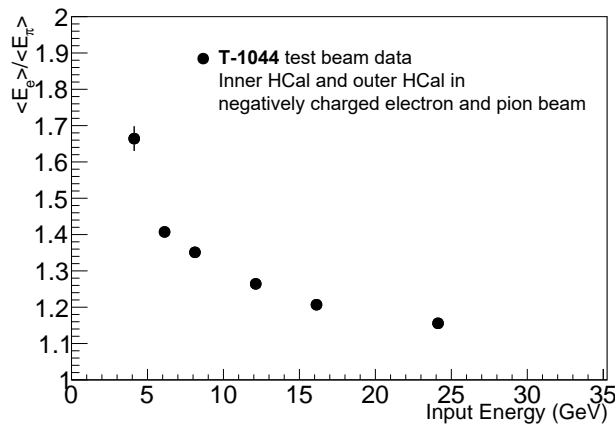

Fig. 29. HCal $\langle E_e \rangle / \langle E_\pi \rangle$ response as function of beam energy.
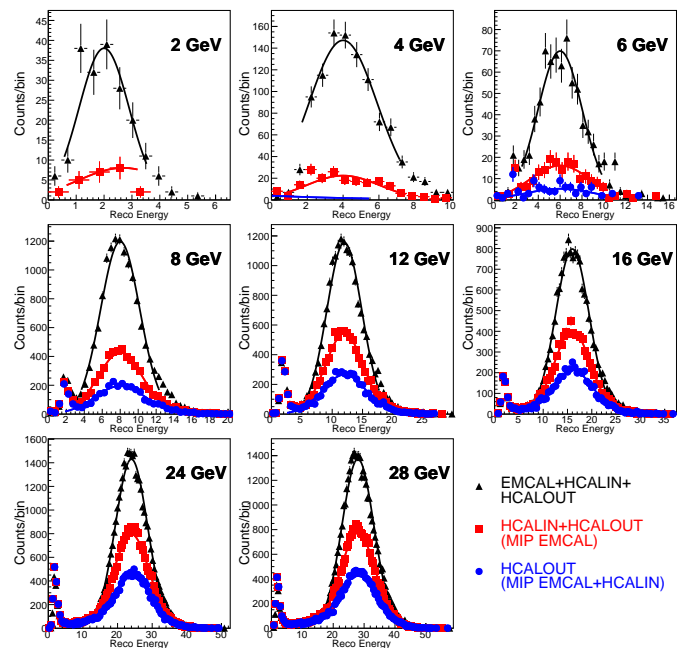

Fig. 30. Hadron energy measurement with combined EMCal+HCal detector. Events were sorted into three categories: 1) HCALOUT where particles pass through the EMCal and inner HCal and then shower in the outer HCal; 2) HCALIN+HCALOUT where particles pass through the EMCal and then shower in either HCal; 3) EMCAL+HCALIN+HCALOUT which includes all showers irrespective of their starting position.

with respect to the beam energy, while the EMCal gain was adjusted for each beam energy separately. Figure 30 shows total reconstructed energy as obtained in Equation (4) for each of the three event categories and various beam energies. The peaks at the lower energy correspond to the small fractions of muon events that pass through the calorimeters leaving only the minimum ionizing energy.

The corresponding hadron resolution is shown in Figure 31 (b). Data are fit in a similar manner with $\Delta E/E = \sqrt{(\delta p/p)^2 + a^2 + b^2/E}$, i.e. with a fixed beam momentum spread term of $\delta p/p \approx 2\%$ subtracted from the constant term in quadrature. HCALOUT showers that pass through the EMCal and inner HCal have a resolution of $17.1\% \oplus 75.5\%/\sqrt{E}$. The p-value for this fit is 0.0041. HCAL showers that pass through through the EMCal have a resolution of $14.5\% \oplus 74.9\%/\sqrt{E}$ which gives a p-value of 0.016 . The combined resolution of all the showers irrespective of their starting position (FULL) is $13.5\% \oplus 64.9\%/\sqrt{E}$ with a p-value of 0.0084 . The hadron resolution improves without the MIP cuts because it reduces the overall shower fluctuations

and leakages.

The linearity is shown in Figure 31 (a). The bottom panel shows the ratio of the measured energy and the corresponding fits. As the FULL data sample is used to adjust the energy sum calibration as in Equation (4), the linear fit coefficient of its measured energy to beam energy is 1 by definition. The same gain factors were applied to the HCAL and HCALOUT shower categories. We qualitatively observed their linearity slope slightly below 1, which could be due to slightly higher energy leakage in those event categories.
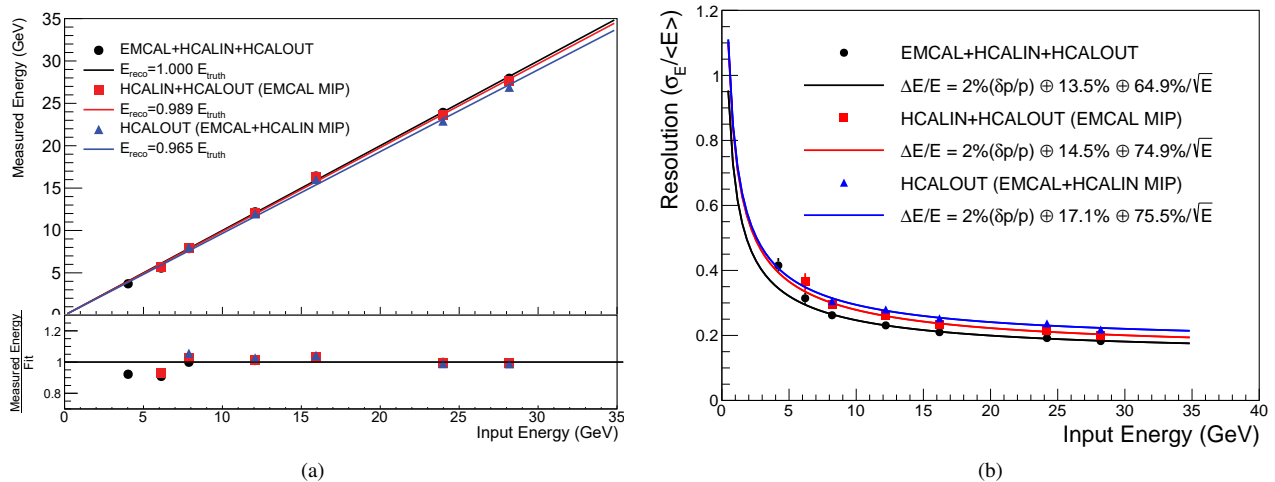
Fig. 31. Hadron (a) linearity and (b) resolution measured with combined EMCal+HCal (sPHENIX configuration) detector setup. Three sets of data points corresponds to the event categories shown in Figure 30. The bottom panel of (a) shows the ratio of the measured energy and corresponding fits.

VIII. CONCLUSIONS

A prototype of the sPHENIX calorimeter system was successfully constructed and tested at the Fermilab Test Beam Facility with beam energies in the range of 1-32 GeV. The energy resolution and linearity of the EMCal and HCal were measured as a combined calorimeter system as well as independently. The energy resolution of the HCal is found to be $\Delta E/E = 11.8\% \oplus 81.1\%/\sqrt{E}$ for hadrons. The energy resolution of EMCal for electrons is $1.6\% \oplus 12.7\%/\sqrt{E}$ for electromagnetic showers that hit at the center of the tower and $2.8\% \oplus 15.5\%/\sqrt{E}$ without the position restriction. Part of the EMCal position dependence of the shower response stems from the non-uniformity of the light collection in the light guide, which will be a major focus of the next stage of detector research and development. The combined hadron resolution of the full EMCal and HCal system for hadrons is $13.5\% \oplus 64.9\%/\sqrt{E}$ and is consistent with the standalone HCal results. All of these results satisfy the requirements of the sPHENIX physics program. Simulation studies are progressing in parallel to support the research and development of these detectors.

C.A. Aidala and M.J. Skoby are with the Department of Physics at the University of Michigan, Ann Arbor, MI 48109-1040.

V. Bailey, J. Blackburn, M.M. Higdon, S. Li, V.R. Loggins, M. Phipps, A.M. Sickles, P. Sobel, and E. Thorsland are with the Department of Physics at the University of Illinois Urbana-Champaign, Urbana, IL 61801-3003.

S. Beckman, R. Belmont, J.L. Nagle, and S. Vazquez-Carson are with the Department of Physics at the University of Colorado Boulder, Boulder, CO 80309-0390.

C. Biggs, S. Boose, M. Chiu, E. Desmond, A. Franz, J.S. Haggerty, J. Huang, E. Kistenev, J. LaBounty, M. Lenz, W. Lenz, E.J. Mannel, C. Pinkenburg, S. Polizzo, C. Pontieri, M.L. Purschke, R. Ruggiero, S. Stoll, A. Sukhanov, F. Toldo, and C.L. Woody are with Brookhaven National Laboratory, Upton, NY 11973-5000.

M. Connors is with the Department of Physics and Astronomy at the Georgia State University, Atlanta, GA 30302-5060 and the RIKEN BNL Research Center, Upton, NY 11973-5000.

X. He and M. Sarsour are with the Department of Physics and Astronomy at the Georgia State University, Atlanta, GA 30302-5060.

K. Kauder is with the Department of Physics and Astronomy at the Wayne State University, Detroit, MI 48201-3718 and Brookhaven National Laboratory, Upton, NY 11973-5000

J.G. Lajoie, T. Rinn, and A. Sen are with the Department of Physics and Astronomy at the Iowa State University, Ames, IA 50011-3160.

T. Majoros and B. Ujvari is with the Institute of Physics at the University of Debrecen, Debrecen, Hungary.

M.P. McCumber is with Los Alamos National Laboratory, Los Alamos, NM 87545-0001.

J. Putschke is with the Department of Physics and Astronomy at the Wayne State University, Detroit, MI 48201-3718.

J. Smiga is with the Department of Physics at the University of Maryland, College Park, MD 20742-4111.

P.W. Stankus is with Oak Ridge National Laboratory, Oak Ridge, TN 37830-8050.

R.S. Towell is with the Department of Engineering and Physics at the Abilene Christian University, Abilene, TX 79699-9000.

REFERENCES

[1] A. Adare *et al.*, "An Upgrade Proposal from the PHENIX Collaboration," *arXiv:1501.06197*, 2015.

[2] E.-C. Aschenauer *et al.*, "The RHIC Cold QCD Plan for 2017 to 2023: A Portal to the EIC," 2016.

[3] K. Adcox *et al.*, "Formation of dense partonic matter in relativistic nucleus nucleus collisions at RHIC: experimental evaluation by the PHENIX collaboration," *Nucl. Phys.*, vol. A757, pp. 184–283, 2005.

[4] J. Adams *et al.*, "Experimental and theoretical challenges in the search for the quark gluon plasma: the STAR collaboration's critical assessment of the evidence from RHIC collisions," *Nucl. Phys.*, vol. A757, pp. 102–183, 2005.

[5] B. B. Back *et al.*, "The PHOBOS perspective on discoveries at RHIC," *Nucl. Phys.*, vol. A757, pp. 28–101, 2005.

[6] I. Arsene *et al.*, "Quark gluon plasma and color glass condensate at RHIC? The perspective from the BRAHMS experiment," *Nucl. Phys.*, vol. A757, pp. 1–27, 2005.

[7] T. G. O'Connor *et al.*, "Design and testing of the 1.5 T superconducting solenoid for the BaBar detector at PEP-II in SLAC," *IEEE Trans. Appl. Supercond.*, vol. 9, pp. 847–851, 1999.

[8] B. D. Leverington *et al.*, "Performance of the prototype module of the GlueX electromagnetic barrel calorimeter," *Nucl. Instrum. Meth.*, vol. A596, pp. 327–337, 2008.

[9] S. A. Sedykh *et al.*, "Electromagnetic calorimeters for the BNL muon (g-2) experiment," *Nucl. Instrum. Meth.*, vol. A455, pp. 346–360, 2000.

[10] T. Armstrong *et al.*, "The E864 lead-scintillating fiber hadronic calorimeter," *Nucl. Instrum. Meth.*, vol. A406, pp. 227–258, 1998.

[11] R. D. Appuhn *et al.*, "The H1 lead / scintillating fiber calorimeter," *Nucl. Instrum. Meth.*, vol. A386, pp. 397–408, 1997.

[12] D. W. Hertzog, P. T. Debevec, R. A. Eisenstein, M. A. Graham, S. A. Hughes, P. E. Reimer, and R. L. Tayloe, "A high resolution lead scintillating fiber electromagnetic calorimeter," *Nucl. Instrum. Meth.*, vol. A294, pp. 446–458, 1990.

[13] T. C. Collaboration, " The CMS Experiment at the CERN LHC ," *JINST*, vol. Vol 3, S08004, pp. 122–155, 2008.

[14] M.Derrick *et al.*, " Design and Construction of the ZEUZ Barrel Calorimeter ," *Nucl. Inst. Meth.*, vol. A309, pp. 77–100, 1991.

[15] S. Bertolucci *et al.*, "The CDF Central and Endwall Hadron Calorimeter," *Nucl. Instrum. Meth.*, vol. A267, pp. 301–314, 1988.

[16] O. Tsai, L. Dunkelberger, C. Gagliardi, S. Heppelmann, H. Huang *et al.*, "Results of R&D on a new construction technique for W/ScFi Calorimeters," *J. Phys. Conf. Ser.*, vol. 404, p. 012023, 2012.

[17] O. D. Tsai *et al.*, "Development of a forward calorimeter system for the STAR experiment," *J. Phys. Conf. Ser.*, vol. 587, no. 1, p. 012053, 2015.

[18] M. P. Materials, "RTV615 Technical Data Sheet," http://www.momentive.com/products/showtechnicaldatasheet.aspx?id=10333, 2016.

[19] 3M, "Vikuiti^TM enhanced specular reflector film (esr)," http://products3.3m.com/catalog/us/en001/electronics_mfg/vikuiti/node_7358GD8CMRbe/root_GST1T4S9TCgv/vroot_S6Q2FD9X0Jge/gvel_B6D4SWL5QCgl/theme_us_vikuiti_3_0/command_AbcPageHandler/output_html, 2010.

[20] Kuraray Corp. Japan, Wavelength Shifting Fibers. Kuraray fibers. accessed: Apr 5, 2017. [Online]. Available: http://kuraraypsf.jp/psf/sf.html

[21] M. Bryant, "Plastic Scintillators For The T2K Fine-Grained Detector," Master's thesis, Department of Physics and Astronomy, British Columbia U., 2007. [Online]. Available: http://www.t2k.org/docs/thesis/localDocDetail?docid=010

[22] W. Anderson *et al.*, "Design, Construction, Operation and Performance of a Hadron Blind Detector for the PHENIX Experiment," *Nucl. Instrum. Meth.*, vol. A646, p. 35, 2011.

[23] M. L. Purschke, "RCDAQ, a lightweight yet powerful data acquisition system," http://www.phenix.bnl.gov/~purschke/rcdaq_doc.pdf, 2012.

[24] M. Backfish, "Meson test beam momentum selection," http://beamdocs.fnal.gov/AD/DocDB/0048/004831/004/DPoverP.pdf, 2016.

[25] The Fermilab test beam facility. accessed: Apr 5, 2017. [Online]. Available: http://ftbf.fnal.gov

[26] N. Feege, "Low-energetic hadron interactions in a highly granular calorimeter," Ph.D. dissertation, Physics Department, Hamburg U., 2011. [Online]. Available: http://www-library.desy.de/cgi-bin/showprep.pl?thesis11-048

[27] M. Blatnik *et al.*, "Performance of a Quintuple-GEM Based RICH Detector Prototype," *IEEE Trans. Nucl. Sci.*, vol. 62, no. 6, pp. 3256–3264, 2015.

[28] R. M. Brown, W. M. Evans, C. N. P. Gee, P. W. Jeffreys, G. N. Patrick, M. D. Rousseau, B. J. Saunders, and M. Sproston, "An Electromagnetic Calorimeter for Use in a Strong Magnetic Field at LEP Based on Ceren 25 Lead Glass and Vacuum Phototriodes," *IEEE Trans. Nucl. Sci.*, vol. 32, pp. 736–740, 1985.

[29] S. Agostinelli *et al.*, "GEANT4: A Simulation toolkit," *Nucl. Instrum. Meth.*, vol. A506, pp. 250–303, 2003.

[30] J. Allison *et al.*, "Geant4 developments and applications," *IEEE Trans. Nucl. Sci.*, vol. 53, p. 270, 2006.

[31] J. B. Birks, "Scintillations from Organic Crystals: Specific Fluorescence and Relative Response to Different Radiations," *Proc. Phys. Soc.*, vol. A64, pp. 874–877, 1951.

[32] M. Hirschberg, R. Beckmann, U. Brandenburg, H. Brueckmann, and K. Wick, "Precise measurement of Birks k_B parameter in plastic scintillators," *IEEE Trans. Nucl. Sci.*, vol. 39, pp. 511–514, 1992.

[33] sPHENIX collaboration, "sphenix software repository," https://github.com/sPHENIX-Collaboration, 2015.

[34] M. Tanabashi *et al.*, "Review of Particle Physics," *Phys. Rev.*, vol. D98, no. 3, p. 030001, 2018.